The long noncoding RNA Charme supervises cardiomyocyte maturation by controlling cell differentiation programs in the developing heart

Valeria Taliani[1‡†], Giulia Buonaiuto[1†], Fabio Desideri[2], Adriano Setti[1], Tiziana Santini[1], Silvia Galfrè[2], Leonardo Schirone[3], Davide Mariani[4], Giacomo Frati[3], Valentina Valenti[3], Sebastiano Sciarretta[3], Emerald Perlas[5], Carmine Nicoletti[6], Antonio Musarò[6], Monica Ballarino[1]

[1]Department of Biology and Biotechnologies "*Charles Darwin*", Sapienza University of Rome, Rome, Italy;

[2]Center for Life Nano- & Neuro-Science of Istituto Italiano di Tecnologia (IIT), 00161, Rome, Italy;

[3]Department of Medical Surgical Sciences and Biotechnologies, Sapienza University of Rome, Latina, Italy;

[4]Center for Human Technologies, Istituto Italiano di Tecnologia (IIT), Genova, Italy;

[5]EMBL-Rome, Epigenetics and Neurobiology Unit, Monterotondo, Italy;

[6]DAHFMO-Unit of Histology and Medical Embryology, Laboratory affiliated to Istituto Pasteur Italia-Fondazione Cenci Bolognetti, Sapienza University of Rome, Rome, Italy.

Corresponding author: Monica Ballarino

e-mail address: monica.ballarino@uniroma1.it; *phone*: +39 06 49912201

[‡]Present address: EMBL, Genome Biology Unit, Heidelberg, Germany

[†]These authors contributed equally to this work

Running Head

Charme functions during development

Key Words

NcRNA; LncRNA; Development; Muscle; Myogenesis; Cardiomyogenesis; Heart

ABSTRACT

Long noncoding RNAs (lncRNAs) are emerging as critical regulators of heart physiology and disease, although the studies unveiling their modes-of-action are still limited to few examples. We recently identified pCharme, a chromatin-associated lncRNA whose functional knockout in mice results in defective myogenesis and morphological remodelling of the cardiac muscle. Here, we combined Cap-Analysis of Gene Expression (CAGE), single-cell (sc)RNA sequencing and whole-mount *in situ* hybridization analyses to study pCharme cardiac expression. Since the early steps of cardiomyogenesis, we found the lncRNA being specifically restricted to cardiomyocytes, where it assists the formation of specific nuclear condensates containing MATR3, as well as important RNAs for cardiac development. In line with the functional significance of these activities, pCharme ablation in mice results in a delayed maturation of cardiomyocytes, which ultimately leads to morphological alterations of the myocardium and ventricular hypo-trabeculation. Since congenital anomalies in myocardium are clinically relevant in humans and predispose patients to major complications, the identification of novel genes controlling cardiac morphology becomes crucial. Our study offers unique insights into a novel lncRNA-mediated regulatory mechanism promoting cardiomyocyte maturation and bears relevance to Charme locus for future theranostic applications.

INTRODUCTION

In all vertebrates, heart development occurs through a cascade of events in which a subtle equilibrium between proliferation, migration, and differentiation ultimately leads precursor cells to mature into all the major cardiac cell types (Bruneau 2013; Moorman and Christoffels 2003). At the molecular level, the execution of the developmental program is governed by the dynamic interplay of several cardiac regulators, whose expression and functions are coordinated in time and space. Alteration of this process results in abnormal cardiac morphogenesis and other congenital heart defects that in humans represent the most common types of birth defects and cause of infant death (Zimmerman et

52 al., 2020; Srivastava, 2006; Center for Disease Control and Prevention, 2020). Mutations of
53 transcription factors and their protein cofactors have emerged as causative of a broad spectrum of
54 heart malformations, although only 15-20% of all congenital heart defects have been associated to
55 known genetic conditions (Morton et al., 2022; Kodo et al., 2009; Bouveret et al., 2015; Ang et al.,
56 2016). The need to find more targets for diagnosis and therapy has therefore evoked interest in new
57 categories of disease-causing genes, whose discovery has been accelerated by impressive
58 advancements in genomics. In this direction, improvements in the next-generation sequencing
59 technologies have revolutionised many areas of the biomedical research, including cardiology, by the
60 discovery of long noncoding RNA (lncRNAs) (Mattick et al., 2004; Cipriano et al., 2018, Rinn and
61 Chang 2012; Ulitsky and Bartel 2013; Yao et al., 2019). LncRNAs form a heterogeneous class of
62 non-protein coding transcripts, longer than 200 nucleotides, participating in many physiological (i.e.
63 cell stemness, differentiation or tissue development) and pathological (i.e. cancer, inflammation,
64 cardiovascular or neurodegeneration) processes (Azad et al., 2021; Hu et al., 2018; Riva et al., 2016).
65 In the heart, several biologically relevant lncRNAs have been identified, with functions related to
66 aging (Jusic et al., 2022) and regeneration (Pagano et al., 2020; Wang et al., 2021). Specifically for
67 cardiac development (Pinheiro et al., 2021), most of the lncRNA-mediated mechanisms were
68 dissected by cell culture studies (Klattenhoff et al., 2013; Ounzain et al., 2015; Kim et al., 2021),
69 while *in vivo* characterizations remained limited to few instances (Grote et al. 2013; Anderson et al.,
70 2016; Ritter et al., 2019; Hazra,R,et al., 2022).
71 The importance of lncRNA for adult heart homeostasis has been often described by linking their
72 aberrant expression to cardiac anomalies (Han et al., 2014; Wang et al., 2016; Ballarino et al., 2018;
73 Han et al., 2019; Ponnusamy et al., 2019; Anderson et al., 2021). Along this line, in 2015 we identified
74 a new collection of muscle-specific lncRNAs (Ballarino et al., 2015) and focused our attention on
75 Charme (Chromatin architect of muscle expression) (mm9 chr7:51,728,798-51,740,770), a
76 mammalian conserved lncRNA gene, whose loss-of-function in mice causes progressive myopathy

77 and, intriguingly, congenital heart remodelling (Ballarino et al., 2018). Here, we look at the function
78 of this lncRNA in a developmental window and assign an embryonal origin to the cardiac defects
79 produced by its knockout. By using molecular and whole-tissue imaging approaches, we give an
80 integrated view of Charme locus activation in the developing heart and show that the functional
81 pCharme isoform, retaining intron-1, is expressed already in the fetal tissues, progressively dropping
82 down after birth. Single-cell (sc)RNA sequencing analyses from available datasets also reveal a
83 strong cell type-specific expression of pCharme in the embryonal heart, where it is restricted to
84 cardiomyocytes (CM). In line with this specific location, high-throughput transcriptomic analyses
85 combined with the phenotypic characterization of WT and Charme^{KO} developing hearts, highlight a
86 functional role of the lncRNA in CM maturation and in the developmental formation of trabeculated
87 myocardium. Furthermore, high-throughput sequencing of RNA isolated from fetal cardiac biopsies
88 upon cross-linking and immunoprecipitation (CLIP) of MATR3, a nuclear pCharme interactor
89 (Desideri et al., 2020), reveals the existence of a specific RNA-rich condensate containing pCharme
90 as well as RNAs for important regulators of embryo development, cardiac function, and
91 morphogenesis. In accordance with the functional importance of the pCharme/MATR3 interaction in
92 developing cardiomyocytes, the binding of these transcripts with MATR3 was altered in Charme^{KO}
93 hearts. Moreover, MATR3 depletion in mouse-derived cardiac primary cells leads to the down-
94 regulation of such RNAs, which suggests an active crosstalk between MATR3, pCharme and cardiac
95 regulatory pathways.
96 Understanding the basics of cardiac development from a lncRNA *point-of-view* is of interest not only
97 for unravelling novel RNA-mediated circuitries but also for improving treatment options aimed at
98 enhancing cardiomyogenic differentiation. Indeed, despite the recent advancements in generating
99 cardiomyocytes from pluripotent stem cells through tissue engineering-based methods, most
100 protocols produce immature cells, which lack many attributes of adult cardiomyocytes (Uosaki et al.,
101 2015). Consequently, the cells generated cannot be used for efficient drug screening, modelling of

102 adult-onset disease, or as a source for cell replacement therapy. We identify here pCharme as a new
103 non-coding regulator of cardiac maturation and characterise the molecular interactome acting with
104 the lncRNA *in vivo*. This research not only advances our understanding of heart physiology but in the
105 next few years may serve as a foundation for new human diagnostic and therapeutic approaches.
106

107 **RESULTS**

108 **Charme locus expression in developing mouse embryos and cardiomyocytes.**

109 Our earlier studies revealed the occurrence of muscle hyperplasia and cardiac remodelling upon the
110 CRISPR/Cas9-mediated Charme loss-of-function in mice (Ballarino et al., 2018; Desideri et al.,
111 2020). Intriguingly, the morphological malformations were clearly displayed in both adult and
112 neonatal mice, strongly suggesting possible roles for the lncRNA during embryogenesis. With the
113 purpose to trace back the developmental origins of Charme functions, we started by analysing the
114 whole collection of FANTOM5 mouse promoterome data to quantify transcription initiation events
115 captured by CAGE-seq across the lncRNA locus (Noguchi et al., 2017). In addition to its cardiac
116 specificity, this profiling revealed the highest expression of the locus during development (E11-E15)
117 followed by a gradual decrease at postnatal stages (**Figure 1A** and **Supplementary File 1**). We then
118 evaluated the expression of the two splice variants, pCharme and mCharme, produced by the locus at
119 E15.5 and postnatally (day 2, after birth). RT-qPCR analyses with specific primers confirmed the
120 CAGE output and revealed that both the isoforms are more expressed at the fetal than the postnatal
121 stage (**Figure 1B**). More importantly, we found pCharme to be 50% more abundant than mCharme,
122 which is particularly intriguing in consideration of the prominent role of the nuclear isoform
123 previously shown in skeletal myogenesis (Desideri et al., 2020). Using *in-situ* hybridization (ISH)
124 approaches, we then profiled by imaging the spatio-temporal expression of Charme during
125 development. These analyses revealed an initial expression of Charme locus already in the tubular
126 heart (**Figure 1C**, E8.5), within territories which will give rise to the future atria and ventricles (V),

127 with the inflow (IFT) and outflow (OFT) tracts displaying the highest signals. ISH also confirmed the
128 expression of the locus at later stages of development, both in cardiac tissues and somites (S) (**Figure**
129 **1C**, E13.5; **Figure 1-figure supplement 1A**). A similar expression pattern was found within intact
130 embryos and fetal hearts by whole-mount *in-situ* hybridization (WISH) (**Figure 1D**). To note, specific
131 signals were detected only in wild-type (Charme^{WT}) heart muscles, whereas no signal was found in
132 Charme knockout organs (Charme^{KO}) (**Figure 1D**, left; **Figure 1-figure supplement 1B**), taken from
133 our previously generated mice (Ballarino et al., 2018). As distinct cell subpopulations are known to
134 form the heart, each one carrying out a specialised function in cardiac development and physiology
135 (de Soysa et al., 2019), we then processed publicly available single-cell RNA sequencing (scRNA-
136 seq) datasets from embryonal hearts (E12.5, Jackson-Weaver et al., 2020) for studying at a deeper
137 resolution the locus expression across individual cell types. Upon clustering (**Figure 1E**, upper) the
138 different cardiac cell-types based on the expression of representative marker genes (Li et al., 2016;
139 Jackson-Weaver et al., 2020; Franco et al., 2006; Meilhac et al., 2018) (**Figure 1-figure supplement**
140 **1C-1E**), we found pCharme expression restricted to cardiomyocytes, with an almost identical
141 distribution between the atrial (CM-A), ventricular (CM-V) and other (CM-VP, CM-IVS, CM-OFT)
142 cell clusters (**Figure 1E**, lower).
143 These findings offered valuable input for exploring the possible integration of pCharme functions
144 into pathways controlling the maturation of cardiomyocytes. In this direction, we analysed *in silico*
145 the lncRNA promoter to search for transcription factors (TFs) acting as upstream regulators of
146 pCharme expression in cardiomyocytes. In accordance with our previous findings (Ballarino et al.,
147 2015), Jaspar database (https://jaspar.genereg.net; Castro-Mondragon et al., 2022) identified several
148 MYOD1 *consensus* sites in the 1kb region upstream of pCharme transcriptional start site (TSS,
149 **Figure 1F)**, although it is known that this myogenic regulator is not expressed in the heart (Olson,
150 1993; Buckingham et al., 2017). To note, a very low number of *consensus* sites was found for
151 ONECUT2, a TF involved in neurogenesis (Aydin et al., 2019). Searching for cardiac regulators, we

152 identified canonical motifs (**Figure 1-figure supplement 1F**) and enriched sites (**Figure 1F**) for the
153 T-box transcription factor-5 (TBX5). In addition to being a key regulator of heart development,
154 known to activate genes associated to CM maturation in early development and morphogenesis at
155 later stages (Nadadur et al., 2016; Steimle et al., 2017), TBX5 was recently found to control the
156 expression of several lncRNAs (Yang et al., 2017), a subset of them intriguingly enriched, as for
157 pCharme, in the chromatin fraction of cardiomyocytes (Hall et al., 2021). By further analysing the
158 scRNA-seq dataset (Jackson-Weaver et al., 2020), we observed a positive and highly significant
159 correlation between *Tbx5* and pCharme (**Figure 1G**, left) in CM, with some differences occurring
160 across the CM cluster subtypes (see for instance CM-IVS/CM-OFT, **Figure 1G**, right). To note,
161 pCharme positively correlates with markers of cardiomyocyte identity, Myosin light chain 2 (*Myl2*)
162 and 4 (*Myl4*), while significant anticorrelation was found for the Kruppel like factor 2 (*Klf2*) and the
163 Twist family BHLH transcription factor 1 (*Twist1*) transcripts, that respectively mark endothelial and
164 neural crest cells (Jackson-Weaver et al., 2020; Li et al., 2016).
165 To provide functional support to a possible role of TBX5 for pCharme transcription in CM, we
166 examined available Chromatin Immunoprecipitation (ChIP)-sequencing (**Figure 1H)** and RNA-seq
167 (**Figure 1I**) datasets from murine cardiomyocytes at progenitor (P-CM) and differentiated (D-CM)
168 stages (Luna-Zurita et al., 2016). In both conditions, ChIP-seq analyses revealed the specific
169 occupancy of TBX5 to highly conserved spots within the pCharme promoter, which increases with
170 differentiation. However, while in differentiated cardiomyocytes pCharme expression was insensitive
171 to TBX5 ablation, the lncRNA abundance was consistently decreased in TBX5 knockout progenitor
172 cells (**Figure 1I**). As progenitor CM represent a cell resource for recapitulating *ex-vivo* the early
173 establishment of the cardiac lineage and for mimicking cardiomyocyte development (Kattman et al.,
174 2011), these results are consistent with the role of TBX5 for Charme transcription at fetal stages. The
175 presence of *consensus* sites for other TFs (**Figure 1-figure supplement 1F)** and the known attitude
176 of TBX5 to interact, physically and functionally, with several cardiac regulators (Akerberg et al.,

177 2019), also predict the possible contribution of other regulators to pCharme transcription which may

178 act, in cooperation or not, with TBX5 during CM maturation.

Figure 1.

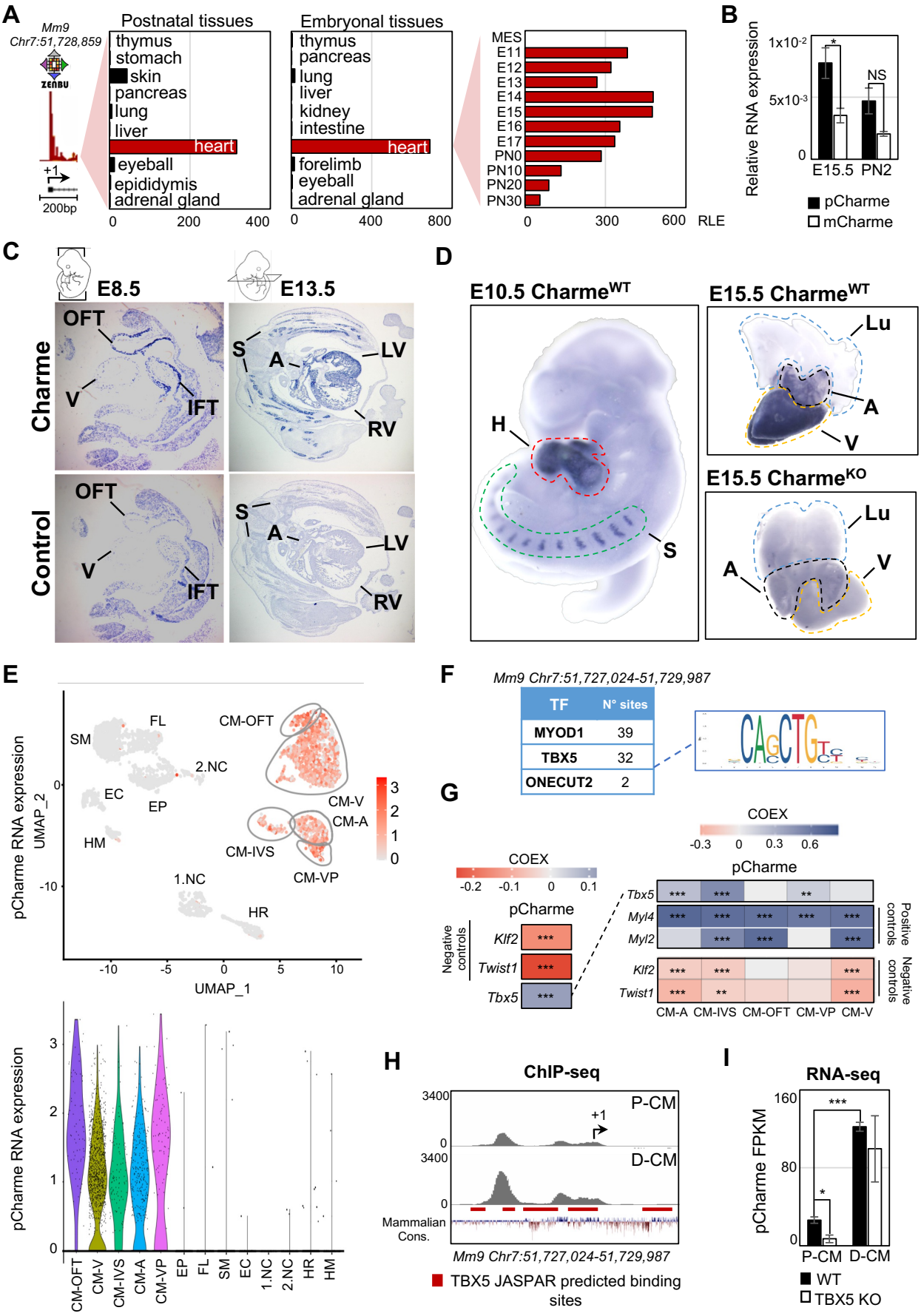
A
Mm9
Chr7:51,728,859
zenbu
+1
200bp
Postnatal tissues
thymus
stomach
skin
pancreas
lung
liver
heart
eyeball
epididymis
adrenal gland
0
200
400
Embryonal tissues
thymus
pancreas
lung
liver
kidney
intestine
heart
forelimb
eyeball
adrenal gland
0
400
800
MES
E11
E12
E13
E14
E15
E16
E17
PN0
PN10
PN20
PN30
0
300
600
RLE
B
Relative RNA expression
1x10-2
5x10-3
0
*
NS
E15.5
PN2
pCharme
mCharme
C
E8.5
E13.5
Charme
Control
OFT
V
IFT
S
A
LV
RV
D
E10.5 CharmeWT
E15.5 CharmeWT
E15.5 CharmeKO
H
S
Lu
A
V
E
pCharme RNA expression
UMAP_2
UMAP_1
SM
FL
CM-OFT
2.NC
EC
EP
HM
CM-V
CM-A
CM-IVS
CM-VP
1.NC
HR
3
2
1
0
-10
-5
0
5
10
pCharme RNA expression
CM-OFT
CM-V
CM-IVS
CM-A
CM-VP
EP
FL
SM
EC
1.NC
2.NC
HR
HM
F
Mm9 Chr7:51,727,024-51,729,987
TF
N° sites
MYOD1
39
TBX5
32
ONECUT2
2
G
COEX
-0.2
-0.1
0
0.1
pCharme
Negative controls
Klf2
Twist1
Tbx5
***
COEX
-0.3
0
0.3
0.6
pCharme
Tbx5
Myl4
Myl2
Klf2
Twist1
Positive controls
Negative controls
CM-A
CM-IVS
CM-OFT
CM-VP
CM-V
H
ChIP-seq
3400
0
P-CM
D-CM
+1
Mammalian Cons.
Mm9 Chr7:51,727,024-51,729,987
TBX5 JASPAR predicted binding sites
I
RNA-seq
pCharme FPKM
160
80
0
***
*
P-CM
D-CM
WT
TBX5 KO

180 **Figure 1. Charme locus expression in developing mouse embryos and cardiomyocytes**

181 **A)** Transcriptional start site (TSS) usage analysis from FANTOM5 CAGE Phase1 and 2
182 datasets (skeletal muscle is not included) on the last update of Zenbu browser
183 (https://fantom.gsc.riken.jp/zenbu/; FANTOM5 Mouse mm9 promoterome)
184 showing Charme locus expression in postnatal and embryonal body districts (left and middle panels)
185 and during different stages of cardiac development (right panel, E11-PN30). MES=Mesoderm. Bars
186 represent the Relative Logaritmic Expression (RLE) of the Tag Per Million values
187 of Charme TSS usage in the specific samples.

188 **B)** Quantitative Reverse Transcription PCR (RT-qPCR) amplification of pCharme and mCharme
189 isoforms in RNA extracts from Charme^{WT} E15.5 and neonatal (PN2) hearts. Data were normalized to
190 *Gapdh* mRNA and represent means ± SEM of 3 pools.

191 **C)** *In-situ* hybridization (ISH) performed on embryonal cryo-sections using digoxigenin-labelled
192 RNA antisense (Charme, upper panel) or sense (control, lower panel) probes against Charme.
193 Representative images from two stages of embryonal development (E8.5 and E13.5) are shown. OFT:
194 Outflow Tract; IFT: Inflow Tract; V: Ventricle; LV/RV: Left/Right Ventricle; A: Atria; S: Somites.

195 **D)** Whole-mount *in-situ* hybridization (WISH) performed on Charme^{WT} intact embryos (E10.5, left
196 panel) and Charme^{WT} and Charme^{KO} hearts at their definitive morphologies (E15.5, right panels).
197 Signal is specifically detected in heart (H, red line) and somites (S, green line). Lungs (Lu, blue line)
198 show no signal for Charme. The specificity of the staining can be appreciated by the complete absence
199 of signal in explanted hearts from Charme^{KO} mice (Ballarino et al., 2018). A: Atria (black line); V:
200 Ventricles (yellow line).

201 **E)** Upper panel: UMAP plot showing pCharme expression in single-cell transcriptomes of embryonal
202 (E12.5) hearts (Jackson-Weaver et al., 2020). Lower panel: Violin plot of pCharme expression in the
203 different clusters (see Materials and Methods for details). CM: Cardiomyocytes, CM-A: Atrial-CM,
204 CM-V: Ventricular-CM, ISV: Interventricular Septum, VP: Venous Pole, OFT: Outflow Tract, NC:

205 Neural Crest cells, EP: Epicardial cells, FL: Fibroblasts like cells, EC: Endothelial Cells, SM: Smooth
206 Muscle cells, HM: Hemopoietic Myeloid cells, HR: Hemopoietic Red blood cells.
207 **F)** *In silico* analysis of MYOD1, TBX5 and ONECUT2 transcription factors (TF) binding
208 sites using Jaspar 2022 (relative profile score threshold=80%) (Castro-Mondragon et al., 2022).
209 MyoD1 and Onecut2 were used as positive and negative controls, respectively. N° sites =number of
210 consensus motifs.
211 **G)** COTAN heatmap obtained using the whole scRNA-seq (left) and contrasted subsetted dataset
212 (right) showing pCharme and *Tbx5* expression correlation (COEX). *Myl4* and *Myl2* were used as
213 positive controls for cardiomyocytes while *Klf2* and *Twist1* as negative controls (markers of EC and
214 NC, respectively). See Materials and Methods for details.
215 **H)** TBX5 ChIP-seq analysis across Charme promoter in murine precursors (P-CM) and differentiated
216 cardiomyocytes (D-CM) (GSE72223, Luna-Zurita et al., 2016). The genomic coordinates of the
217 promoter, the Charme TSS (+1, black arrow), the TBX5 JASPAR predicted binding sites
218 (red lines) and the mammalian conservation track (Mammalian Cons.) from UCSC genome browser
219 are reported.
220 **I)** Quantification of pCharme expression from RNA-seq analysis performed in wild type (WT) and
221 TBX5 knockout (KO) murine P-CM and D-CM (SRP062699, Luna-Zurita et al., 2016). FPKM:
222 Fragments Per Kilobase of transcript per Million mapped reads.
223 Data information: *p < 0.05; ***p < 0.001; NS > 0.05, unpaired Student's t-test.
224
225 **Genome-wide profiling of cardiac Charme^{WT} and Charme^{KO} transcriptomes**
226 Over the years, we have accumulated strong evidence on the role played by pCharme in skeletal
227 myogenesis (Ballarino et al., 2018; Desideri et al., 2020), however important questions are still
228 pending on the role of pCharme in cardiomyogenesis. As a first step towards the identification of the
229 molecular signature underlying Charme-dependent cardiac anomalies, we performed a differential

230 gene expression analysis on transcriptome profiles from Charme^{WT} and Charme^{KO} neonatal (PN2)
231 hearts (**Figure 2A**; **Figure 2-figure supplement 1A**). At this stage, the heart continues to change
232 undergoing maturation, a process in which its morphology and cell composition keep evolving
233 (Padula et al., 2021; Tian et al., 2017).
234 RNA-seq analysis of whole hearts led to the identification of 913 differentially expressed genes
235 (DEGs) (FDR<0.1, WT *vs* KO, **Supplementary File 2**), 573 of which were Up-regulated and 340
236 were Down-regulated in Charme^{KO} hearts (**Figure 2B**; **Supplementary File 2**). These results were
237 confirmed by RT-qPCR analyses performed on gene subsets from independent biological replicates
238 (**Figure 2C**; **Figure 2-figure supplement 1B**). Similar to pCharme activity in skeletal myocytes
239 (Ballarino et al., 2018), we did not find DEGs within the neighbouring chromatin environment (370
240 Kb around Charme) (**Figure 2-figure supplement 1C**).
241 A Gene Ontology (GO) term enrichment study was then applied separately to the Up- and Down-
242 regulated DEGs. These analyses revealed that the Up-regulated DEGs were primarily enriched (FDR-
243 values < 1,0E-10) in cell cycle and cell division categories (**Figure 2D**, left panel), which parallels
244 with a slight increase in the number of KI-67^{+} mitotic Charme^{KO} nuclei, as quantified from neonatal
245 cardiac sections (**Figure 2-figure supplement 1D**). The same study applied to the Down-regulated
246 DEGs revealed their enrichment to more functional and morphogenetic GO categories and primarily
247 referred to anatomical structure morphogenesis (FDR 5.77E-07) and circulatory system development
248 (FDR 3.1338E-06) (**Figure 2D,** right panel). Interestingly, these top-ranked categories include TFs
249 involved in pivotal steps of embryo development, such as *Smad3* (Dunn et al., 2004) and *Nocth3*
250 (MacGrogan et al., 2018), and functional components of cardiomyocytes, such as the voltage-
251 dependent calcium channel subunit *Cacna1c* (Wang et al., 2018), and Myosin-18B (*Myo18B*), known
252 to regulate cardiac sarcomere organisation (Latham et al., 2020). By expanding the analysis of these
253 genes from neonatal to embryonal timepoints (E12.5, E15.5 and E18.5), we found that their
254 expression significantly decreases upon pCharme ablation from the fetal E15.5 stage onward, as

255 compared to WT (**Figure 2E**). Similarly, the *Myh6*/*Myh7* ratio, which measures CM maturation
256 (England and Loughna, 2013; Scheuermann and Boyer, 2013) and that increases over the wild-type
257 timepoints, displays a gradual decrease in the Charme^{KO} hearts from E15.5 onward (**Figure 2F**). To
258 note, the expression of cell-cycle and proliferation genes was not affected by pCharme ablation over
259 the same developmental window (**Figure 2-figure supplement 1E**). Hence, their upregulation in
260 neonatal KO hearts could be due to the impairment of cardiac maturation, which leads to a shift to a
261 more fetal and proliferative state of cardiomyocytes upon birth.
262 Overall, our findings suggest that during cardiac development, pCharme regulation is achieved
263 through the regulation of morphogenetic pathways whose dysregulation causes a pathological
264 remodelling of the heart. Accordingly, histological analyses performed by haematoxylin and eosin
265 staining of Charme^{WT} and Charme^{KO} cardiac cryo-sections (E15.5) showed a pronounced alteration
266 of the myocardium, with a clear decrease of the area of the ventricular cavities (**Figure 2G**). The
267 histological investigation was then deepened to the trabeculated myocardium, the tissue directly
268 surrounding ventricle cavities. To this purpose, we performed immunofluorescence staining and
269 western blot analysis for the natriuretic peptide A (NPPA) factor, a known marker of the embryonal
270 trabecular cardiomyocytes (Choquet et al., 2019; Horsthuis et al., 2008). In parallel, heart sections
271 were analysed for cardiac vasculature, since i) the process of trabeculae formation is known to be
272 temporally coupled with the formation of blood vessels during development (Samsa et al., 2013) and,
273 importantly, ii) the "circulatory system development" category was among the main GO enriched for
274 pCharme down-regulated targets. We found that, with respect to WT, mutant hearts display a
275 significant reduction of NPPA^{+} trabeculae (**Figure 2H; Figure 2- figure supplement 1F**), which
276 parallels the decreased expression of the *Irx3* and *Sema3a* trabecular markers (Choquet et al., 2019)
277 (**Figure 2-figure supplement 1G**) as well as the diminished density of the capillary endothelium, as
278 imaged by lectin staining (**Figure 2-figure supplement 1H**). Therefore, the fetal expression of
279 pCharme is necessary for the achievement of morphogenetic programs important for CM maturation,

myocardial geometry and vascular network formation. Overall, these ensure the preservation of the cardiac function and structure in adulthood, as a progressive deterioration of the systolic function, which becomes significant at 9 months of age (**Figure 2-figure supplement 1I**; **Supplementary File 3**), was observed in Charme^{KO} mice. To note, a similar alteration in heart efficiency was observed in the murine model with a specific mutation in the pCharme intron-1 (Charme$^{\Delta Int}$) (Desideri et al., 2020), further confirming the distinct activity of this isoform in cardiac processes.

Figure 2

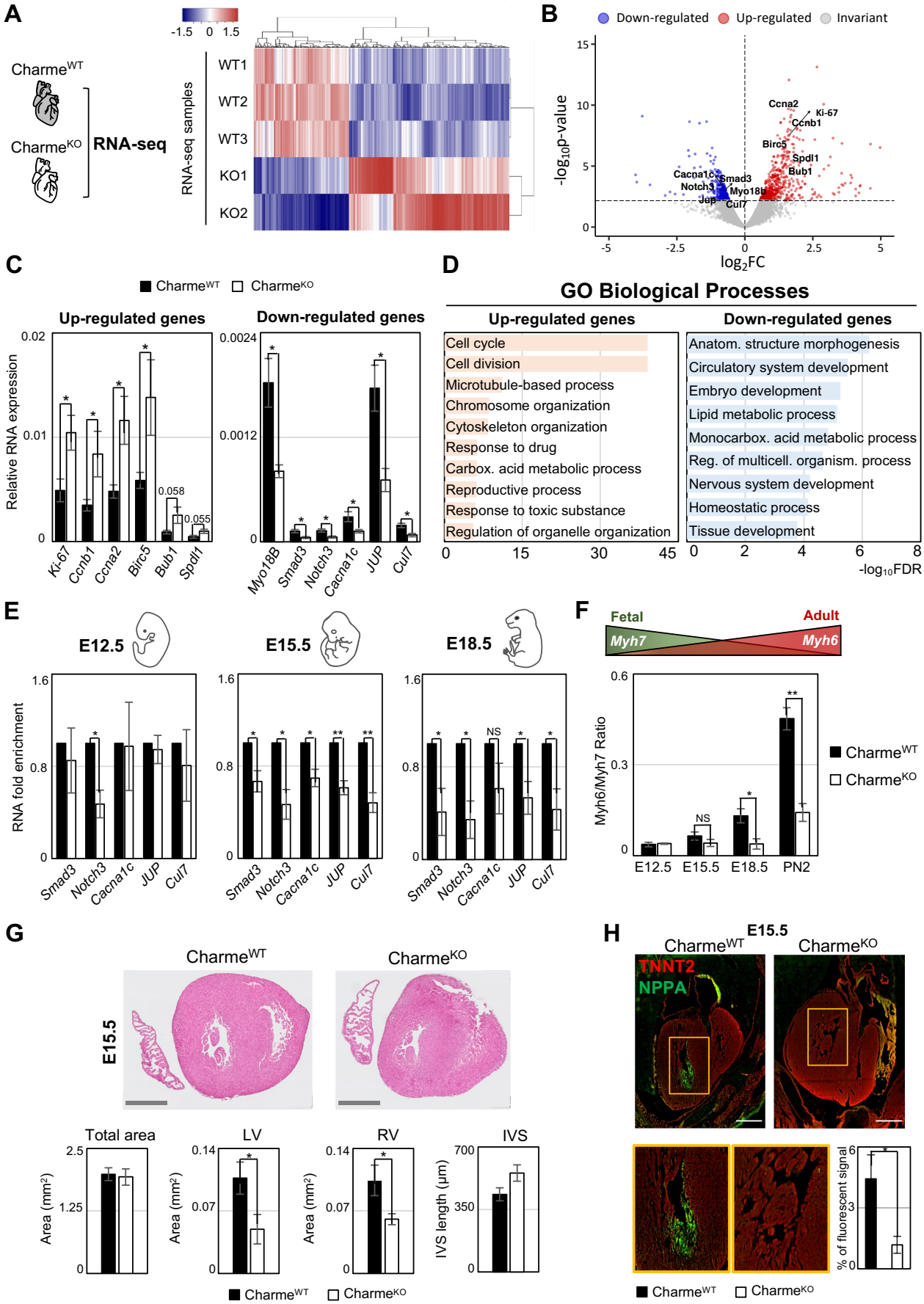
A
Charme^WT
Charme^KO
RNA-seq
RNA-seq samples
WT1
WT2
WT3
KO1
KO2
-1.5 0 1.5
B
Down-regulated
Up-regulated
Invariant
-log10p-value
log2FC
Ccna2
Ki-67
Ccnb1
Birc5
Spdl1
Bub1
Cacna1c
Notch3
Smad3
Myo18b
Jup
Cul7
C
Charme^WT
Charme^KO
Up-regulated genes
Down-regulated genes
Relative RNA expression
Ki-67
Ccnb1
Ccna2
Birc5
Bub1
Spdl1
Myo18B
Smad3
Notch3
Cacna1c
JUP
Cul7
0.058
0.055
D
GO Biological Processes
Up-regulated genes
Cell cycle
Cell division
Microtubule-based process
Chromosome organization
Cytoskeleton organization
Response to drug
Carbox. acid metabolic process
Reproductive process
Response to toxic substance
Regulation of organelle organization
Down-regulated genes
Anatom. structure morphogenesis
Circulatory system development
Embryo development
Lipid metabolic process
Monocarbox. acid metabolic process
Reg. of multicell. organism. process
Nervous system development
Homeostatic process
Tissue development
-log10FDR
E
E12.5
E15.5
E18.5
RNA fold enrichment
Smad3
Notch3
Cacna1c
JUP
Cul7
NS
F
Fetal
Adult
Myh7
Myh6
Myh6/Myh7 Ratio
E12.5
E15.5
E18.5
PN2
Charme^WT
Charme^KO
G
Charme^WT
Charme^KO
E15.5
Total area
LV
RV
IVS
Area (mm²)
IVS length (µm)
Charme^WT
Charme^KO
H
E15.5
Charme^WT
Charme^KO
TNNT2
NPPA
% of fluorescent signal
Charme^WT
Charme^KO

286

287 **Figure 2. Genome-wide profiling of cardiac Charme^{WT} and Charme^{KO} transcriptomes**

288 **A)** Heatmap visualization from RNA-seq analysis of Charme^{WT} and Charme^{KO} neonatal (PN2) hearts.
289 Plot was produced by heatmap3 (https://cran.r-
290 project.org/web/packages/heatmap3/vignettes/vignette.pdf). Expression values were calculated as
291 FPKM, were $\log_2$-transformed and mean-centered. FPKM: Fragments Per Kilobase of transcript per
292 Million mapped reads.

293 **B)** Volcano plots showing differential gene expression from transcriptome analysis of Charme^{WT} *vs*
294 Charme^{KO} PN2 hearts. Differentially expressed genes (DEGs) validated through RT-qPCR (**Figure**
295 **2C**) are in evidence. FC: Fold Change

296 **C)** RT-qPCR quantification of Up-regulated (left panel) and Down-regulated (right panel) DEGs in
297 Charme^{WT} *vs* Charme^{KO} neonatal hearts. Data were normalized to *Gapdh* mRNA and represent means
298 ± SEM of WT (n=5) *vs* KO (n=4) pools

299 **D)** Gene Ontology (GO) enrichment analysis performed by WEBGESTALT
300 (http://www.webgestalt.org) on Up-regulated (left panel) and Down-regulated (right panel) DEGs in
301 Charme^{WT} *vs* Charme^{KO} pools of neonatal hearts. Bars indicate the top categories of Biological
302 processes in decreasing order of $-\log_{10}$FDR. All the represented categories show a False Discovery
303 Rate (FDR) value <0.05.

304 **E)** RT-qPCR quantification of pCharme targets in Charme^{WT} and Charme^{KO} extracts from E12.5,
305 E15.5 and E18.5 hearts. DEGs belonging to the GO category "anatomical structure morphogenesis"
306 were considered for the analysis. Data were normalized to *Gapdh* mRNA and represent means ± SEM
307 of WT and KO (n=3) pools.

308 **F)** RT-qPCR quantification of the Myh6/Myh7 ratio in Charme^{WT} and Charme^{KO} extracts from E12.5,
309 E15.5 and E18.5 and neonatal hearts. Data were normalized to *Gapdh* mRNA and represent means ±
310 SEM of WT and KO (n=3) pools. Schematic representation of the physiological *Myh6*/*Myh7*
311 expression trend is shown.

312 **G)** Upper panel: Haematoxylin-eosin staining from Charme^{WT} and Charme^{KO} E15.5 cardiac
313 transverse sections. Scale bars: 500 µm. Lower panel: Quantification of the total area, the left and
314 right ventricle cavities and the thickness of the interventricular septum (IVS) in Charme^{WT} and
315 Charme^{KO} E15.5 hearts. For each genotype, data represent the mean ± SEM (n=3).
316 **H)** Representative images of Nppa (green) and TnnT2 (red) immunostaining in Charme^{WT} and
317 Charme^{KO} (E15.5) cardiac sections. Regions of interest (ROI, orange squares) were digitally enlarged
318 on the lower panels. Scale bar: 500 µm. Quantification of the area covered by the Nppa fluorescent
319 signal is shown aside. Data represent the mean (%) ± SEM of WT (n=4) and KO (n=3).
320 Data information: *$p < 0.05$; **$p < 0.01$, NS > 0.05, unpaired Student's t-test
321
322 **pCharme nucleates the formation of RNA-rich condensates by interacting with MATR3 in fetal**
323 **cardiomyocytes.**
324 In differentiated myocytes, we previously demonstrated that CU-rich binding motifs inside pCharme
325 coordinate the co-transcriptional recruitment and the subcellular localization of Matrin 3 (MATR3)
326 (Desideri et al., 2020), a nuclear matrix RNA/DNA binding protein involved in multiple RNA
327 biosynthetic processes (Coelho et al., 2016; Banerjee et al., 2017) and recently shown to play a role
328 in chromatin repositioning during development (Cha et al., 2021). Interestingly, MATR3 was found
329 highly expressed in cardiomyocytes from newborn mice and heterozygous mutations in MATR3
330 resulted in congenital heart defects (Quintero-Rivera et al., 2015). This raises the intriguing
331 possibility that pCharme may play a role in cardiomyocyte maturation through MATR3. To examine
332 this hypothesis, we first assessed the subcellular localization of pCharme in fetal (E15.5) hearts by
333 biochemical fractionation. RT-qPCR analyses revealed that, in line with what was previously
334 observed in skeletal muscle, in cardiomyocytes pCharme mainly localises in the nucleus, while the
335 fully spliced mCharme is enriched in the cytoplasm (**Figure 3-figure supplement 1A**). We next
336 applied high-resolution RNA-fluorescence *in situ* hybridization (RNA-FISH) to visualise pCharme

337 alone (**Figure 3A**; **Figure 3-figure supplement 1B**) or relatively to MATR3 through a combined
338 immunofluorescence IF/RNA-FISH approach (**Figure 3B**). In agreement with the subcellular
339 fractionation, the imaging experiments confirmed the nuclear localization of pCharme, which exhibits
340 its typical punctuate pattern. Further analysis of the three-dimensional distribution of pCharme and
341 MATR3 revealed a clear colocalization of their signals and the formation of nuclear condensates, as
342 quantified by 3D Pearson's correlation coefficient applied on the overlapping signals (**Figure 3-**
343 **figure supplement 1C**). Based on these results, we then tested if the presence of pCharme could
344 influence the nuclear localization of MATR3. To this end, we performed MATR3 IF assays in wild-
345 type and Charme^{KO} fetal (E15.5) muscle biopsies and in spinal cord nuclei (**Figure 3C**; **Figure 3-**
346 **figure supplement 1D-F**). A striking heterogeneous distribution of MATR3 positive signals was
347 observed within the nucleus of wild-type skeletal (**Figure 3-figure supplement 1D**) and cardiac
348 (**Figure 3C**, upper panel) muscles, both expressing the lncRNA. Coherently with their pCharme-
349 dependent formation, these condensates appeared more diffuse in tissues where the lncRNA is not
350 expressed, as Charme^{KO} muscles and WT spinal cords (**Figure 3C**, middle and lower panels; **Figure**
351 **3-figure supplement 1D**). More accurate quantification of the MATR3 fluorescence distribution in
352 the nucleus of Charme^{KO} cardiomyocytes (Coefficient of variation (CV), **Figure 3-figure**
353 **supplement 1F**), revealed a MATR3 IF pattern which was less discrete and more homogeneous in
354 respect to WT.

Figure 3

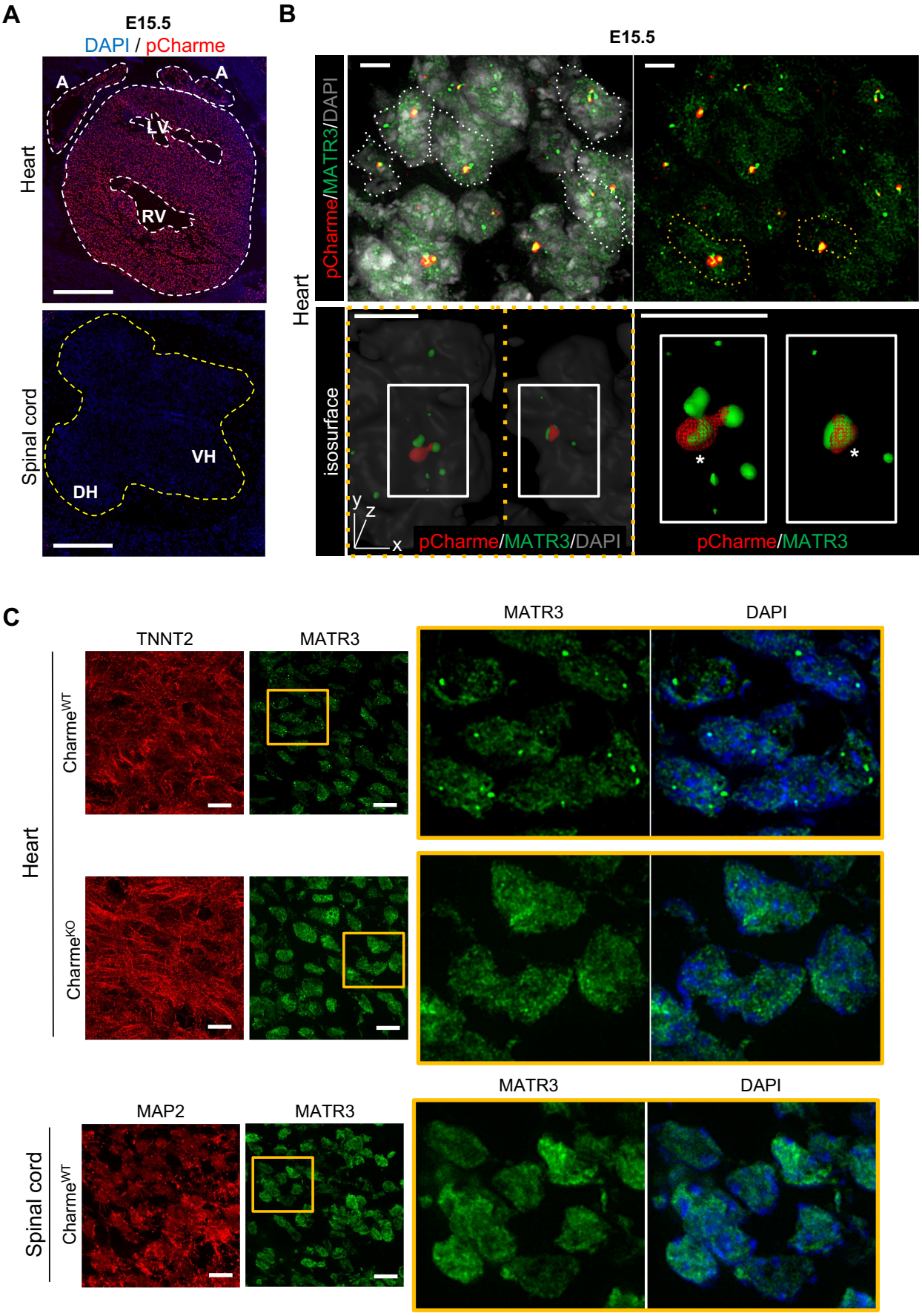
A
E15.5
DAPI / pCharme
Heart
A
A
LV
RV
Spinal cord
VH
DH
B
E15.5
Heart
pCharme/MATR3/DAPI
isosurface
y
z
x
pCharme/MATR3/DAPI
pCharme/MATR3
C
TNNT2
MATR3
MATR3
DAPI
Heart
CharmeWT
CharmeKO
MAP2
MATR3
MATR3
DAPI
Spinal cord
CharmeWT

355

356 **Figure 3. In fetal cardiomyocytes pCharme nucleates the nuclear localization of MATR3**

357 **A)** RNA-FISH for pCharme (red) and DAPI staining (blue) in Charme^{WT} cardiac and spinal cord
358 from E15.5 tissue sections. Whole heart (white dashed lines), spinal cord (yellow dashed line). A:
359 Atria; LV and RV: Left and Right ventricle; DH and VH: Dorsal and Ventral Horn. Scale bars, 500
360 µm.

361 **B)** Upper panel: RNA-FISH for pCharme (red) combined with immunofluorescence for MATR3
362 (green) and DAPI staining (gray) in Charme^{WT} from E15.5 cardiac sections. Dashed lines show the
363 edge of nuclei. Lower panel: selected nuclei (yellow dashed lines in the upper panel) were enlarged
364 and processed for isosurface reconstruction (left panel) and digital magnification (right panel).
365 Overlapped signals are shown (asterisks). Scale bars, 5 µm.

366 **C)** Upper panel: Representative images for MATR3 (green), TnnT2 (red) and DAPI (blue) stainings
367 on Charme^{WT} and Charme^{KO} E15.5 cardiac sections. Lower panel: Representative images for for
368 MATR3 (green), Map2 (red) and DAPI (blue) stainings on Charme^{WT} and Charme^{KO} E15.5 spinal
369 cord sections. ROI (orange squares) were digitally enlarged on the right panels. Each image is
370 representative of three individual biological replicates. Scale bars, 10 µm.

371

372 The known ability of MATR3 to interact with both DNA and RNA and the high retention of pCharme
373 on the chromatin may predict the presence of chromatin and/or specific transcripts within these
374 MATR3-enriched condensates. In skeletal muscle cells, we have previously observed on a genome-
375 wide scale, a global reduction of MATR3 chromatin binding in the absence of pCharme (Desideri et
376 al., 2020). Nevertheless, the broad distribution of the protein over the genome made the identification
377 of specific targets through MATR3-ChIP challenging. With the purpose to functionally characterise
378 MATR3 interactome, here we applied a more straightforward MATR3 cross-linking
379 immunoprecipitation (CLIP)-seq approach to fetal Charme^{WT} and Charme^{KO} hearts for the
380 identification of MATR3 bound RNA targets (**Figure 4A**). Western blot analyses with antibodies

381 against MATR3 allowed to test the efficiency of protein recovery after the immunoprecipitation, in
382 both the WT and KO conditions (**Figure 4-figure supplement 1A**). Subsequent analysis of the RNA,
383 led to the identification of 951 cardiac-expressed transcripts significantly bound by MATR3 in the
384 WT heart (log2 Fold enrichment >2 and FDR value <0.05, **Figure 4-figure supplement 1B** and
385 **Supplementary File 4**). Four candidates (*Cacna1c*, *Myo18B*, *Tbx20*, *Gata4*) were selected based on
386 their FDR values (**Supplementary File 4**) for further validation by RT-qPCR, together with *Gapdh*
387 as a negative control (**Figure 4-figure supplement 1C**).
388 In line with the binding propensities exhibited by MATR3 in other cell systems (Uemura et al., 2017),
389 most of its enrichment was located within the introns of protein-coding mRNA precursors (**Figure**
390 **4B**). Strikingly, even though the class of lncRNAs was poorly represented (**Figure 4B**, upper panel),
391 we found pCharme at the top of the MATR3 interactors in Charme^{WT} hearts (**Supplementary File**
392 **4**). Quantification of the retrieved RNAs by RT-qPCR evidenced the specific enrichment of pCharme
393 but not mCharme in the wild-type samples, which supports the distinctive binding of MATR3 to the
394 nuclear isoform (**Figure 4-figure supplement 1D**). As expected, we observed a strong reduction of
395 MATR3-CLIP signal on Charme RNA in Charme^{KO} samples (**Figure 4C**, **Supplementary File 4**).
396 To gain further insight into the specificity of MATR3 binding, we proceeded with the analysis of the
397 CLIP-identified peaks for the identification of RNA-binding proteins consensus sites, including
398 MATR3. Motif enrichment analysis using 93 RNA-binding motifs catalogued by CISBP-RNA
399 database (Ray D, et al., 2013) pinpointed the MATR3 consensus sequence (UUCUU, Desideri et al.,
400 2020) among the most over-represented pyrimidine-enriched motifs (Evalue < 0.05) (**Figure 4D**).
401 When analysed in respect to the intensity of the CLIP signals, the MATR3 motif was positioned at
402 the peak summit (+/- 50 nt) (**Figure 4E**), close to the strongest enrichment of MATR3, further
403 confirming a direct and highly specific binding of the protein to these sites. Upon this quality
404 assessment, we finally performed a GO enrichment analysis on the 882 protein-coding transcripts
405 directly bound by MATR3 in the WT heart and found "Heart development" as the most significantly

406 enriched functional category (**Figure 4F**). Therefore, our results indicate the formation of MATR3-
407 containing condensates inside the nucleus of cardiomyocytes which contain pCharme, as the most
408 abundant lncRNA, and pre-mRNA encoding for important cardiac regulators.

Figure 4

A

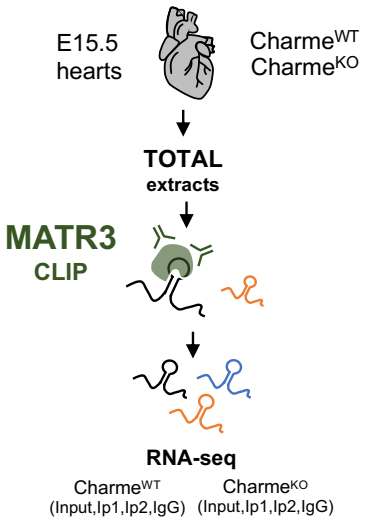

B

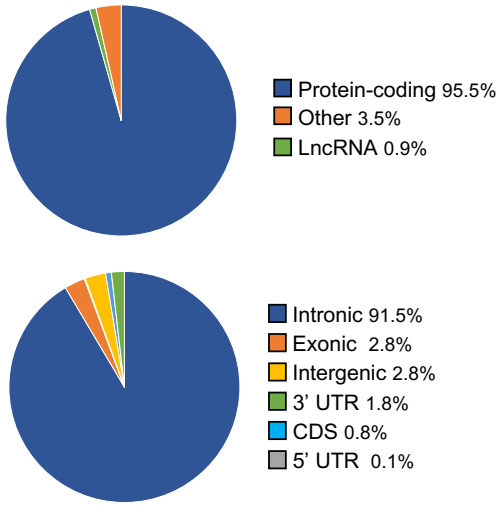

C

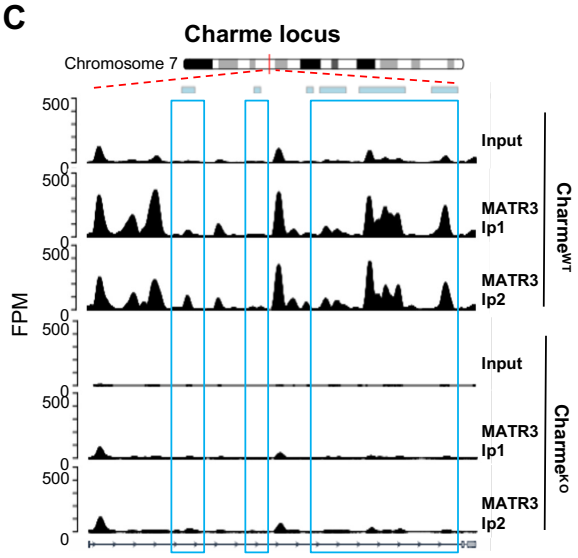

D

Motif enrichment analysis

Motif	Motif ID	Protein name	E-Value
	M207 0.6	PCBP1	$4.40e^{-26}$
	M043 0.6	PCBP2	$2.17e^{-22}$
	Desideri et al.,2020	MATR3	$1.48e^{-17}$
	M228 0.6	PTBP1	$1.18e^{-16}$
	M188 0.6	PCBP3	$2.03e^{-16}$
	M227 0.6	ROD1	$3.43e^{-14}$
	M037 0.6	MBNL1	$1.49e^{-5}$

E

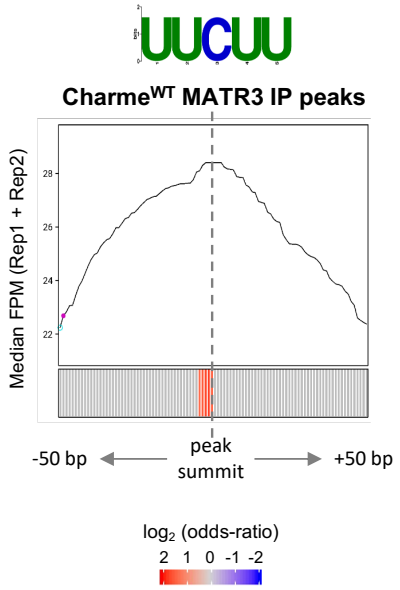

F

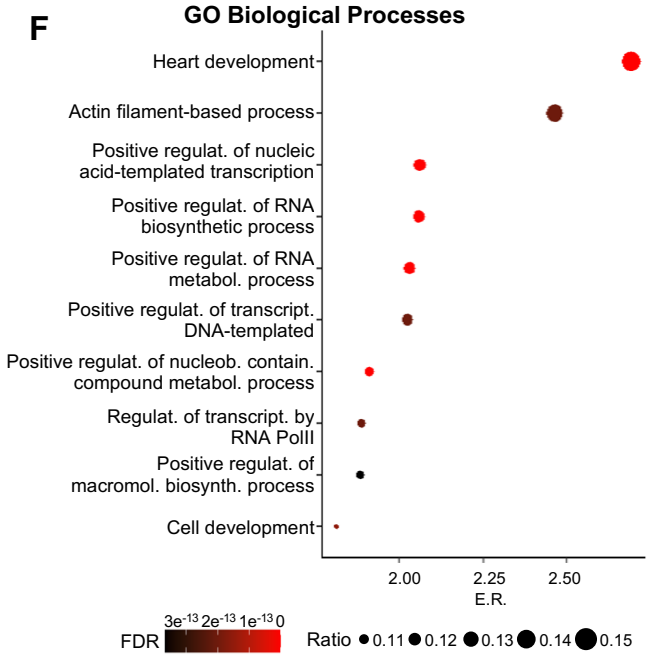

410

411 **Figure 4. MATR3/pCharme nuclear condensates contain key regulators of heart development**

412 **A)** Schematic representation of MATR3 CLIP-seq workflow from fetal (E15.5) Charme^{WT} and

413 Charme^{KO} hearts. See **Materials and Methods** for details.

414 **B)** MATR3 CLIP-seq from fetal hearts. Upper panel: a pie-plot projection representing transcript

415 biotypes of 951 identified MATR3 interacting RNAs. Peaks overlapping multiple transcripts were

416 assigned with the following priority: protein coding, lncRNA and others. Lower panel: a pie-plot

417 projection representing the location of MATR3 enriched peaks (log2 Fold enrichment > 2 and FDR

418 < 0.05). Peaks overlapping multiple regions were assigned with the following priority: CDS, 3'UTR,

419 5'UTR, exons, introns and intergenic. Percentages relative to each group are shown.

420 **C)** MATR3 CLIP-seq (Input, Ip1 and Ip2) normalized read coverage tracks (FPM) across pCharme

421 from fetal hearts. Significant MATR3 peaks, displaying $\log_2$ Fold enrichment > 2 in both Ip1 and Ip2

422 samples compared to Input, are demarcated by light-blue boxes.

423 Normalized read coverage tracks (FPM) from MATR3 CLIP-seq in Charme^{KO} fetal hearts on Charme

424 locus are also shown. Plot obtained using Gviz R package.

425 **D)** Motif enrichment analysis perfomed on MATR3 CLIP-seq peaks (Charme^{WT}) with AME software

426 using 93 RNA binding motifs from CISBP-RNA database. 7 consensus motifs resulted significantly

427 over-represented (Evalue < 0.05) among the MATR3 peaks, as compared to control regions. See

428 **Material and Methods** for details.

429 **E)** Positional enrichment analysis of MATR3 motif in MATR3 CLIP-seq peaks (Charme^{WT}). For

430 each analyzed position close to peak summit, line plot displays the median CLIP-seq signal (FPM,

431 IP1 + IP2), while heatmap displays the log2 odds-ratio of UUCUU motif enrichment. Significant

432 enrichments (p-value < 0.05) are shown in red. See **Material and Methods** for details.

433 **F)** GO enriched categories obtained with WebGestalt (http://www.webgestalt.org) on protein-coding

434 genes overlapping Charme^{WT} MATR3 peaks. Dots indicate the top categories of biological processes

435 (description in y-axis) in decreasing order of Enrichment Ratio (E.R.= overlapped genes/expected
436 genes, x-axis). Dot size (Ratio) represents the ratio between overlapped gens and GO categories size
437 while dot color (FDR) represents significance. All the represented categories show an FDR<0.05.
438

439 **The pCharme/MATR3 interaction sustains developmental gene expression in fetal**
440 **cardiomyocytes.**

441 On a transcriptome scale, we found that in the heart the expression of MATR3-bound RNAs was
442 globally reduced by pCharme knockout (**Figure 5-figure supplement 1A**). Indeed, while MATR3
443 targets were under-represented among transcripts whose expression was unaffected (invariant) or
444 increased (up-regulated) by pCharme ablation, 12% of the downregulated DEGs (41 out of 340) were
445 bound by MATR3 (**Figure 5A**). To note, these common targets were significantly enriched across
446 the top-three GO classes, previously defined for Charme^{KO} downregulated genes (**Figure 5B**). This
447 evidence suggests that pCharme is needed to sustain the cardiac expression of MATR3 targets. To
448 investigate the possible implication of the lncRNA for MATR3 binding to RNA, we proceeded with
449 a differential binding (DB) analysis of MATR3 CLIP-seq datasets between Charme^{WT} and Charme^{KO}
450 conditions (**Figure 5-figure supplement 1B**,**C**). Among the shared peaks, DB revealed that the main
451 consequence of pCharme depletion was a significant decrease of MATR3 enrichment on the RNA
452 (**Figure 5C**, Loss), while the increase of protein binding was observed on a lower fraction of peaks
453 (**Figure 5C**, Gain). In line with the specificity for MATR3 binding, also in these sets of differentially
454 bound regions, the MATR3 motif was positioned close to the summit of the peak (**Figure 5-figure**
455 **supplement 1D**). By mapping these differentially bound regions to the MATR3 targets which are
456 also responsive to pCharme ablation (DEGs), we found that while the gained peaks were equally
457 distributed, the loss peaks were significantly enriched in a subset (20 out of 40, 50%) of down-
458 regulated DEGs (**Figure 5D**, upper panel). Overall, these results suggest that cooperation between
459 pCharme and MATR3 activities is needed for the expression of specific RNAs, which majority (13

460 out of 20) is known to play important roles in embryo development, anatomical structure
461 morphogenesis and development of the circulatory system (**Figure 5D**, lower panel). Indeed, we
462 found interesting candidates such as *Cacna1c*, *Notch3*, *Myo18B* and *Rbm20*, whose role in cardiac
463 physiopathology was extensively studied (Goonasekera et al., 2012; Tao et al., 2017; Ajima et al.,
464 2008; van den Hoogenhof et al., 2018).
465 Finally, to univocally distinguish the contribution of pCharme and MATR3 on their expression, we
466 tested the effect of MATR3 depletion on the abundance of these RNAs. We then purified cardiac
467 primary cells from wild-type hearts for transfection with control (si-SCR) or MATR3 (si-*Matr3*)
468 siRNAs (**Figure 5E**, left panel). RT-qPCR analysis revealed that 3 out of 4 tested genes exhibited a
469 significant expression decrease upon MATR3 depletion (**Figure 5E**, right panel).
470 In sum, these data offer unprecedented knowledge on the RNA-binding propensities of MATR3 in
471 the fetal heart and identify a subset of RNAs whose expression and MATR3 binding are influenced
472 by pCharme. Our results demonstrate that in the developing heart RNA-rich MATR3-condensates
473 form at the sites of pCharme transcription and control the expression of important regulators of
474 embryo development, cardiac function, and morphogenesis. To the best of our knowledge, no
475 previous research has given such an insight into the importance of specific lncRNA/RNA binding
476 protein interactions occurring at the embryonal stages of mammalian heart development. As MATR3
477 is involved in multiple nuclear processes, further studies will be necessary to address how the early
478 interaction of the protein with pCharme impacts on the expression of specific RNAs, either at
479 transcriptional or post-transcriptional stages.

Figure 5

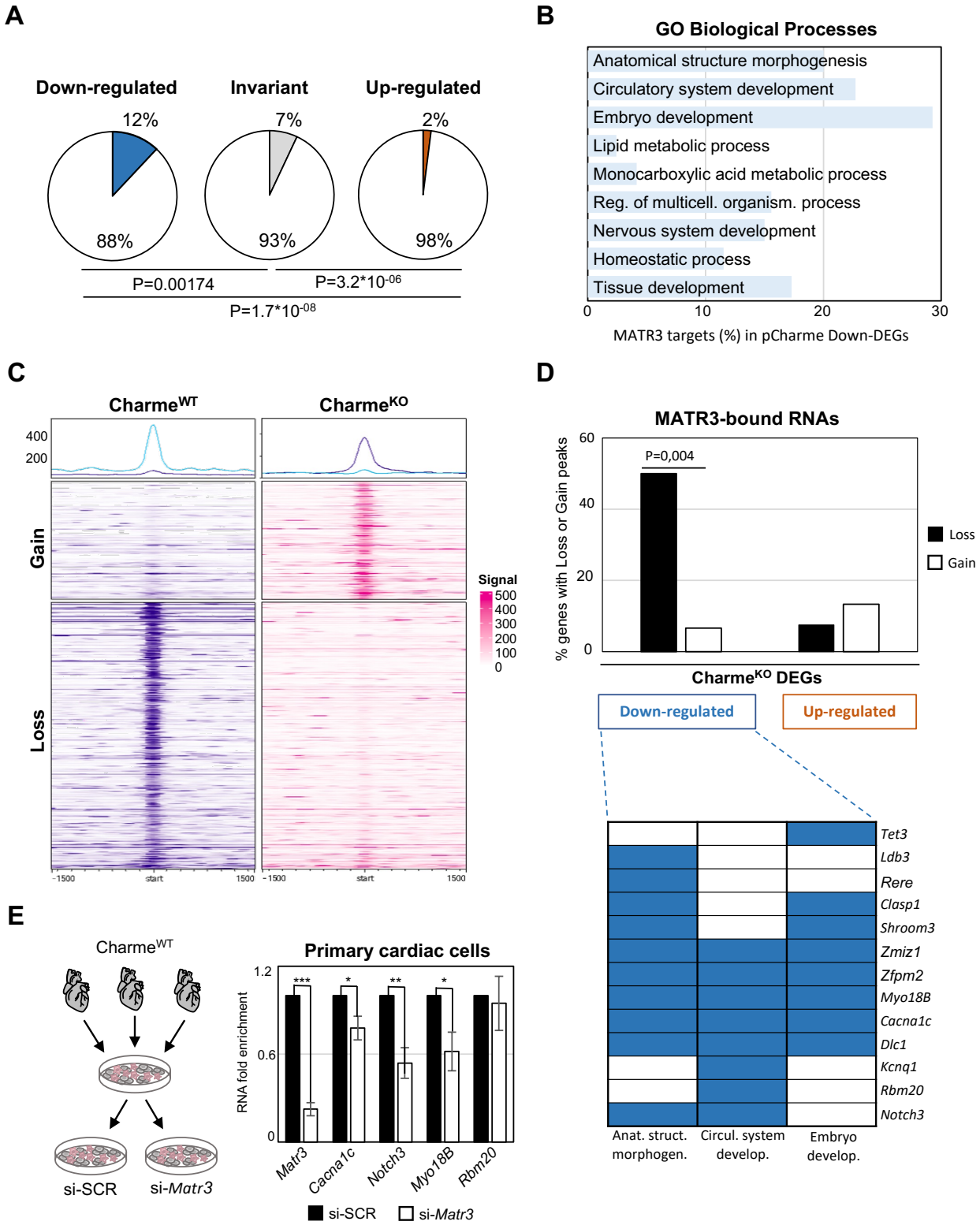

Figure 5. The pCharme/MATR3 interaction in cardiomyocytes sustains developmental genes expression

483 **A)** Pie charts showing the percentage of MATR3 targets in Charme^{KO} down-regulated, invariant or
484 up-regulated DEGs. Significance of enrichment or depletion was assessed with two-sided Fisher's
485 Exact test, shown below.
486 **B)** MATR3 targets (%) in the GO categories enriching Charme^{KO} down-regulated DEGs (Down-
487 DEGs) (see also **Figure 2A**).
488 **C)** Profile Heatmaps of differential MATR3 CLIP-seq peaks (Charme^{WT} *vs* Charme^{KO}). Normalized
489 mean read counts of both IP samples are shown only for significant (FDR < 0.05) «Gain» and «Loss»
490 peaks.
491 **D)** Upper panel: histogram showing the distribution (%) of «Gain» and «Loss» MATR3 peaks in
492 pCharme DEGs. Significance of enrichment was assessed with two-sided Fisher's Exact test. Lower
493 panel: distribution of the subset (13 out of 20) of Down-DEGs with Loss peaks in the first three GO
494 categories identified for down-regulated genes (see also Figure 2A).
495 **E)** Left panel: Schematic representation of primary cells extraction from Charme^{WT} hearts. Once
496 isolated, cells were plated and transfected with the specific siRNA (si-*Matr3*) or control siRNA (si-
497 SCR). See Materials and Methods for details. Right panel: RT-qPCR quantification of *Matr3*,
498 *Cacna1c*, *Notch3*, *Myo18B* and *Rbm20* RNA levels in primary cardiac cells treated with si-SCR or
499 si-*Matr3*. Data were normalized to *Gapdh* mRNA and represent mean ± SEM of 4 independent
500 experiments. Data information: *p < 0.05; **p < 0.01; ***p < 0.001, unpaired Student's t test.
501

502 **DISCUSSION**

503 In living organisms, the dynamic assembly and disassembly of distinct RNA-rich molecular
504 condensates influences several aspects of gene expression and disease (Roden et al., 2021). The
505 engagement of specific lncRNAs can enhance the biochemical versatility of these condensates
506 because of the extraordinary tissue-specificity, structural flexibility and the propensity of this class
507 of RNAs to gather macromolecules (Buonaiuto et al., 2021). Furthermore, the maintenance of specific

508 lncRNAs on the chromatin combined with their scaffolding activity for RNA and proteins can
509 cunningly seed high-local concentrations of molecules to specific loci (Bhat et al., 2021; Ribeiro et
510 al., 2018). The occurrence of alternative RNA processing events eventually leads to the formation of
511 diverse lncRNA isoforms, thus refining the biochemical properties and the binding affinities of these
512 ncRNAs. This suggestive model perfectly fits with pCharme and provides mechanistic insights into
513 the physiologic importance of this lncRNA in muscle. In fact, of the two different splicing isoforms
514 produced by the Charme locus, only the unspliced and nuclear pCharme isoform was found to play
515 an epigenetic, architectural function in skeletal myogenesis under physiological circumstances.
516 Here, we took advantage of our Charme^{KO} mouse model to extend the characterization of the lncRNA
517 in embryogenesis. We show that the temporal and cell-type specific expression of pCharme is critical
518 for the activation of pro-differentiation cardiac genes during development. Mechanistically, we
519 provide evidence that this activity relies on the formation of pCharme-dependent RNA-rich
520 condensates acting as chromatin hubs for MATR3, a nuclear matrix DNA/RNA-binding protein
521 highly abundant in the fetal heart and source, upon mutation, of congenital defects (Quintero-Rivera
522 et al., 2015). MATR3 ability to bind RNA can lead to the formation of dynamic shell-like nuclear
523 condensates, whose composition depends on the integrity of the two RNA Recognition Motifs
524 (RRM1 and 2) (Malik et al., 2018, Sprunger et al., 2022). Evidence supporting the physiological
525 relevance of RNA-MATR3 interplay is emerging in both neural and muscle pathologies (Ramesh Net
526 al., 2020; Senderek J, et al. 2009; Feit H, et al 1998.). In skeletal muscle, we previously showed that
527 the presence of an intronic element bearing ~100 MATR3 binding sites inside pCharme, is needed
528 for MATR3 nuclear localization (Desideri et al., 2020). Here, we add an important dowel into the
529 functional characterization of pCharme and give a developmental meaning to its interaction with
530 MATR3 (**Figure 6**). We show that the absence of the lncRNA in cardiomyocytes alters the MATR3
531 nuclear distribution and its binding to specific RNAs, with a consequent mis-regulation of their
532 developmental expression. Among them, we found a subset of shared pCharme/MATR3 targets,

533 whose role in cardiac physiopathology was extensively studied, such as *Smad3*, *Notch3* and the
534 myogenic components *Cacna1c* and *Myosin-18B* (Goonasekera et al., 2012; Tao et al., 2017; Ajima
535 et al., 2008; van den Hoogenhof et al., 2018).

Figure 6

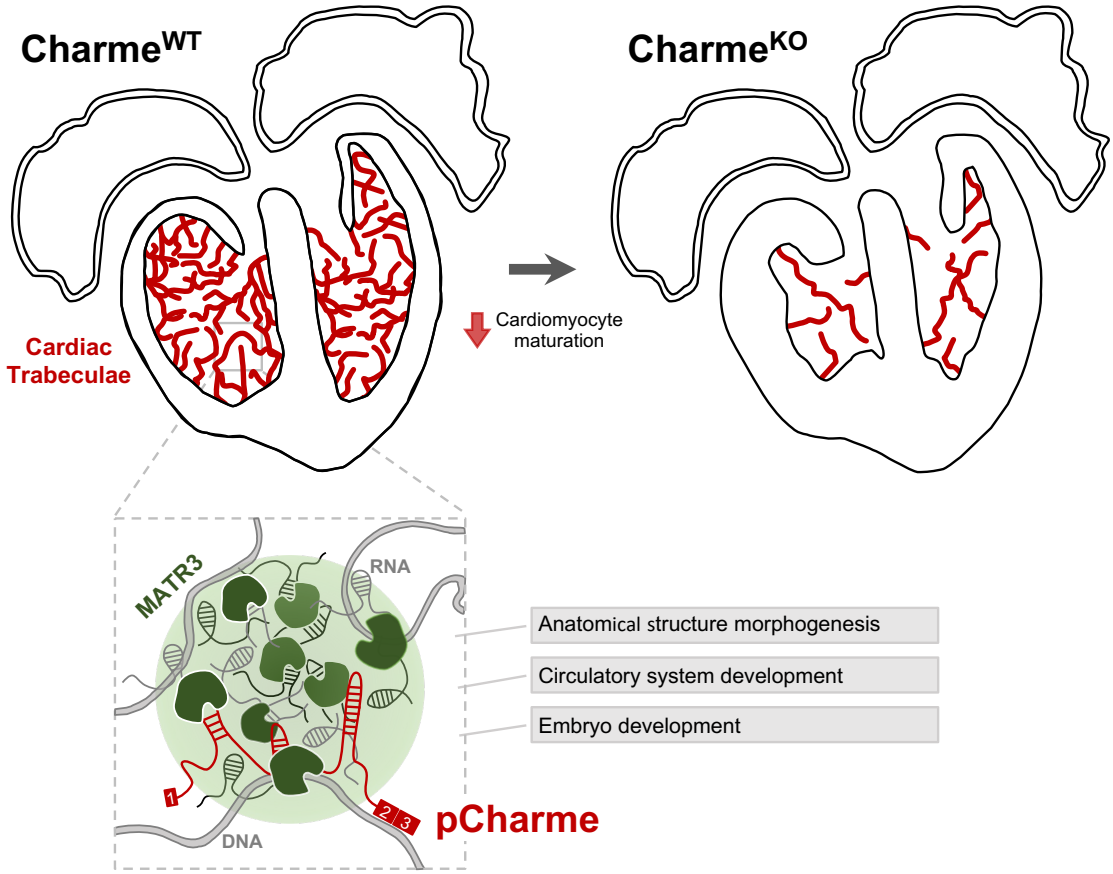

536

537 **Figure 6. Proposed model for pCharme functions during heart development**.
538 At developmental stages (Charme^{WT}), pCharme is required for the expression of genes involved in
539 cardiomyocyte maturation. This activity is accompanied by the formation of nuclear condensates,
540 through the interaction with the RNA-binding protein MATR3, which enrich transcripts involved in
541 cardiac development. pCharme absence (Charme^{KO}) leads to the reduction of cardiac trabeculae
542 during development and to the remodelling of heart morphology.

543

544 It is interesting to note that, in the cardiac context, the reactivation of fetal-specific RNA-binding
545 proteins, including MATR3, was recently found to drive transcriptome-wide switches through the

546 regulation of early steps of RNA transcription and processing (D'Antonio et al., 2022). Along this
547 view, the pCharme-dependent regulation of MATR3 binding in developing cardiomyocytes
548 emphasises the need of cell-type specific lncRNAs for ruling the protein activities to specific RNAs,
549 in a tissue-distinctive and spatio-temporal manner. As the impairment in the nuclear distribution of
550 MATR3 can exert adverse effects in diverse tissues, our study may provide a more inclusive
551 viewpoint on myopathies as well as other neuromuscular disorders where alteration in muscle
552 development involves not only the myogenic lineage but also the interaction of the myogenic cells
553 with the surrounding tissues.
554 These results also underlie the importance of studying cardiomyogenesis in animal models, which
555 allow a better appreciation of the balance between the proliferation and maturation processes in
556 cardiomyocytes and, importantly, the study of the cardiac functions in adulthood. In our case, adult
557 Charme^{KO} mice develop a significant reduction of systolic function with initial signs of cardiac
558 dilation, which denotes an early phase of cardiomyopathy. The results are supported by recently
559 published data suggesting that the transition of cardiomyocytes toward an immature phenotype *in*
560 *vivo* is associated with the development of dilated cardiomyopathy (Ikeda et al., 2019).
561 Recent cardiovascular studies have uncovered essential roles for lncRNAs in cardiac development
562 and disease (Scheuermann and Boyer, 2013; Anderson et al., 2016; Ritter et al., 2019). However, a
563 still unmet need is to disentangle non-canonical lncRNA-mediated mechanisms of action to gain
564 insight into more successful diagnosis and classification of patient subpopulation but also to use them
565 as possible diagnostic biomarkers or therapeutic targets (Buonaiuto et al., 2021). Future efforts will
566 be devoted to clarifying the implication of the syntenic pCharme transcript in those human
567 cardiomyopathies where pathological remodelling of the cardiac muscle occurs.
568

569 **MATERIALS AND METHODS**

570 **Ethics Statement and animal procedures**

571 C57BI/6J mice were used in this work. The Charme^{KO} animals were previously derived through the
572 insertion of a PolyA signal in the Charme locus, as detailed in (Ballarino et al., 2018). All procedures
573 involving laboratory animals were performed according to the institutional and national guidelines
574 and legislations of Italy and according to the guidelines of Good Laboratory Practice (GLP). All
575 experiments were approved by the Institutional Animal Use and Care Committee and carried out in
576 accordance with the law (Protocol number 82945.56). All animals were kept in a temperature of 22°C
577 ± 3°C with a humidity between 50% and 60%, in animal cages with at least 5 animals.
578

579 **Isolation, transfection, and subcellular fractionation of mouse primary heart cells**

580 For primary heart cells isolation and transfection, 5 to 10 postnatal (PN3) hearts for each replicate
581 (n=4) were pooled, harvested and kept at 37°C in culture medium (FBS 10%, 1X Non-Essential
582 aminoacids, 1x PenStrep and DMEM high glucose). Hearts were mashed with pestles for 2 min and
583 cell isolation performed according to manufacturer's instructions (Neonatal Heart Dissociation Kit,
584 Miltenyi Biotec). Cell suspension was centrifuged for 5 min at 600 x g and cells were resuspended in
585 cell culture medium and plated in 22.1 mm plates. 1,5 million cells were transfected 48 hr later with
586 75 mM si-SCR or si-MATR3 in 3 µl/ml of Lipofectamine RNAiMAX (Thermo Fisher Scientific) and
587 100 µl/ml of Opti-MEM (Thermo Fisher Scientific), according to manufacturer's specifications. Total
588 RNA was collected 48 hr after transfection. See **Supplementary File 5** for siRNA sequences.
589 Subcellular fractionation of primary embryonal (E15.5) cardiac cells was performed using the Paris
590 Kit (Thermo Fisher Scientific, cat#AM1921), according to the manufacturer's instructions.
591

592 **Whole-mount *in situ* hybridization**

593 Embryos were fixed overnight in 4% paraformaldehyde (PFA) in phosphate-buffered saline (PBS)
594 plus 0.1% Tween® 20 (PBT) at 4°C, dehydrated through a series of methanol/PBT solutions (25%,
595 50%, 75% and 100% methanol), and stored at -20°C until hybridization. Fixed embryos were

596 rehydrated and rinsed twice in PBT. At this point, embryos were either digested with DNase and/or
597 RNase or kept in PBT. All embryos were bleached in 6% hydrogen peroxide in PBT for 1h. Embryos
598 were then rinsed 3 times in PBT for 5 min, digested with proteinase K (10 µg/ml in PBT) for 5 min
599 at room temperature, washed once in 2 mg/ml glycine in PBT and twice in PBT for 5 min each, and
600 post-fixed in 4% PFA/0.2% glutaraldehyde in PBT for 20 min at room temperature. Embryos were
601 subsequently rinsed twice in PBT for 5 min and pre-hybridized at 70°C in hybridization solution
602 (50% Formamide, 5x SSC, pH 5, 0.1% Tween 20, 50 µg/ml heparin, 50 µg/ml Torula RNA, 50 µg/ml
603 salmon sperm DNA) for 2h. Embryos were then incubated overnight at 70°C in hybridization solution
604 containing 500 ng/ml of denatured riboprobe. Riboprobes were generated by *in vitro* transcription in
605 the presence of Digoxigenin-UTP (Roche Diagnostics). Antisense and sense Charme probes, used as
606 specificity controls, were synthesised from linearized pBluescript-Charme_Ex2/3 plasmid. On the
607 second day, embryos were washed twice in 50% formamide/4x SSC, pH 5/1% SDS and twice in 50%
608 formamide/2x SSC, pH 5 for 30 min each at 55°C. Embryos were then rinsed three times for 5 min
609 in MABT (100 mM maleic acid, 150 mM NaCl, pH 7.5, 0.1% Tween), blocked for 2 h at room
610 temperature in 10% goat serum in MABT, and incubated overnight at 4°C in 1% goat serum in MABT
611 with 1:5000 alkaline phosphatase-coupled anti-Digoxigenin antibody (Roche Diagnostics). On the
612 third day, embryos were washed in MABT twice for 5 min and 5 more times for 1 h each. Embryos
613 were then rinsed twice in NTMT (100 mM NaCl, 100 mM Tris-HCl, pH 9.5, 50 mM MgCl2, 0.1%
614 Tween) for 15 min each, followed by the staining reaction in BM Purple (Roche Diagnostics) in the
615 dark for 30 min to 12 h. Stained embryos were fixed overnight in 4% PFA in PBT, stored in PBT and
616 photographed under a stereomicroscope.
617

618 **Cryo-section *in situ* hybridization**

619 Embryos were dissected in cold PBS (pH 7.4) and fixed in 4% w/v PFA for 24 h at 4°C. Following
620 fixation, the embryos were cryoprotected either in 30% w/v sucrose in PBS (for PFA-fixed embryos)

621 or in 30% w/v sucrose in 0.1 M Tris pH 7.5 (for Z7-fixed embryos), embedded in tissue freezing
622 medium (Leica Microsystems), sectioned at 12 µm using a cryostat (Leica 1900UV) and transferred
623 to superfrost plus (ROTH) slides. The sections were air-dried for at least 30 min and stored at −80°C
624 until later use. For chromogenic detection, sections were post-fixed in 4% w/v PFA in PBS for 10
625 min or in Z7, washed three times in PBS (or twice in 0.1 M Tris–HCl pH:7, 0.05 M NaCl and once
626 in PBS for Z7) and incubated in acetylating solution (1.3% v/v triethanolamine, 0.03 N HCl, 0.25%
627 v/v acetic anhydrite) for 10 min. Sections were then washed in PBS, incubated in 1% v/v Triton-X-
628 100 in PBS for 30 min and washed three times in PBS. Prehybridization was performed for 4-6 h in
629 buffer H (50% v/v formamide, 5× SSC (0.75 M NaCl, 0.075 M sodium citrate), 5× Denhardt's (0.1%
630 bovine serum albumin, 0.1% and 0.1% Polyvinylpyrrolidone), 250 µg/ml yeast RNA and 500 µg/ml
631 salmon sperm DNA). Hybridization was performed in a humidified chamber for 16 h at 65°C in H
632 buffer with DIG-labeled probe added (400 µg/ml). The probes were generated by *in vitro* transcription
633 in the presence of Digoxigenin-UTP (Roche Diagnostics). Following hybridization, sections were
634 sequentially washed in 5× SSC (5 min, 65°C), 0.2× SSC (1 h, 65°C), 0.2× SSC (5 min, RT). Then
635 they were incubated in AB buffer (0.1 M Tris pH 7.5, 0.15 M NaCl) for 5 min, and in blocking
636 solution (10% v/v Fetal Calf Serum in AB) for 1–2 h at RT. Antibody incubation was performed for
637 16 h at 4°C in AB buffer supplemented with 1% v/v Fetal Calf Serum and anti-DIG antibody coupled
638 to alkaline phosphatase (1:5000 dilution; Roche). Sections were then washed thoroughly in AB and
639 equilibrated in alkaline phosphatase buffer (AP - 0.1 M Tris–HCl pH: 9.5, 0.1 M NaCl, 0.05 M
640 MgCl2) for 5 min. Alkaline phosphatase activity was detected in the dark in AP buffer supplemented
641 with 45 mg/ml 4-nitrobluetetrazolium chloride (NBT, Roche) and 35 mg/ml 5-bromo-4-chloro-3-
642 indolyl-phosphate (BCIP, Roche). The reaction was stopped with PBS and the sections were mounted
643 in Glycergel (Dako). Sections were analysed and photographed under a stereomicroscope.
644 Fluorescent detection was performed via Basescope™ assay (Advanced Cell Diagnostics, Bio-
645 Techne) as previously described in D'Ambra et al., 2021, with little modifications according to the

646 manufacturer's instructions for tissue processing. Probes used to specifically detect pCharme RNA
647 (ref. 1136321-C1) were custom produced by Advanced Cell Diagnostics and designed to specifically
648 target the intronic sequence in order to detect the unspliced transcripts.
649
650 **Preparation of probe templates for *in-situ* hybridization experiments**
651 pCharme exon 2 and exon 3 were PCR-amplified from cDNA extracted from myotubes using
652 Charme_Up-BamHI and Charme_Down-EcoRI primers (**Supplementary File 5**). PCR products
653 were cloned into pBluescript ks(-) upon BamHI and EcoRI (Thermo Fisher Scientific) enzymatic
654 restriction.
655
656 **Histology**
657 All hearts were fixed in 4% formaldehyde, embedded in OCT, and cut into 7 µm sections. After
658 washing with PBS 3 times for 5 min, the sections were stained for 7 min with eosin (Merk,
659 cat#109844). Subsequently, slides were washed 3 times with PBS and then incubated with
660 haematoxylin (Merk, 105175) for 90 s.
661
662 **Immunohistochemistry**
663 Fresh E15.5 and PN tissues were embedded in OCT and then frozen in isopentane pre-chilled in liquid
664 nitrogen. Cryo-sections (10 µm of thickness) were fixed in PFA 4% at 4°C for 20 min prior staining
665 with primary antibodies, as previously described. Antibodies and dilutions are reported in
666 **Supplementary File 5**. DAPI, KI-67, NPPA, TNNT2 and G. simplicifolia lectin immunofluorescence
667 signals (Figure 2H; Figure 2-figure supplement 1D,E,H) were acquired with Carl Zeiss Microscopy
668 GmbH Imager A2 equipped with Axiocam503 color camera. MATR3, TNNT2 and MAP2 signals
669 (Figure 3C; Figure 3-figure supplement 1D,E) were acquired as Z stacks (200 nm path) by inverted
670 confocal Olympus IX73 microscope equipped with a Crestoptics X-LIGHT V3 spinning disk system

671 and a Prime BSI Express Scientific CMOS camera. Images were acquired as 16bit 2048x2048 pixel
672 file by using 100X NA 1.40 and 60X NA 1.35 oil (UPLANSApo) objectives and were collected with
673 the MetaMorph software (Molecular Devices). The average number of KI-67 positive nuclei from
674 n=4 Charme^{WT} and Charme^{KO} neonatal cardiac sections was determined by dividing the number of
675 immunolabeled nuclei over the total number of nuclei in each microscope field. For each replicate,
676 from 4 to 18 fields were analysed with ImageJ Software (Schneider C.A. et al., 2012). NPPA and G.
677 simplicifolia lectins sub-tissutal staining (Figure 2H; Figure 2-figure supplement 1H) was analysed
678 using ImageJ software (Schneider C.A. et al., 2012) and according to Fukuda et al., 2013, with little
679 modifications. Briefly, we quantified the ratio between the area covered by the NPPA/lectins signal
680 immunofluorescence signals and the total area of the left ventricle. To calculate the area, the left
681 ventricle was selected with the line selection tool. A threshold was then applied to the selected region
682 to measure the area covered by the signal. Plot in Fig. 2F represents the percentage of area covered
683 by the NPPA/lectins signal divided by the area of the left ventricle.
684 Quantification of MATR3 puncta in Figure 3C was performed using ImageJ software (Schneider C.A.
685 et al., 2012) according to (Higaki T. et al., 2020), with little modifications. Briefly, a "mask" from
686 binarized images was created and used to measure the intensity of MATR3 fluorescence inside the
687 nuclei and the standard deviation (SD). MATR3 distribution was evaluated by Coefficient Variation
688 (CV) defined as CV= mean SD/mean MATR3 intensity. A higher CV value indicates a higher spatial
689 variability of fluorescence distribution (punctate staining); conversely, a lower CV value corresponds
690 to a higher uniformity of fluorescence distribution (diffuse staining). Statistical analysis was
691 performed using t-test, and the differences between means were considered significant at $P \leq 0.05$.
692

693 **RNA extraction and RT-qPCR analysis**

694 Total RNA from cultured cells and tissues was isolated using TRI Reagent (Zymo Research),
695 extracted with Direct-zol™ RNA MiniPrep (Zymo Research), treated with DNase (Zymo Research),

696 retrotranscribed using PrimeScript Reagent Kit (Takara) and amplified by RT-qPCR using PowerUp
697 SYBR-Green MasterMix (Thermo Fisher Scientific), as described in Desideri et al., 2020. See
698 Supplementary File 5 for oligos details.
699
700 **RNA-Seq Analysis**
701 To reduce biological variability, Charme^{WT} and Charme^{KO} neonatal littermates (PN2) were sacrificed
702 and hearts from the corresponding genotypes pooled together before RNA extraction (3 Charme^{WT}
703 pools, 9 hearts each, 2 Charme^{KO} pools, 3 hearts each). Validation analyses were performed on 2
704 additional Charme^{WT} pools (6 hearts each) and 2 Charme^{KO} pools (4 hearts each). Principal
705 component analysis (PCA) conducted on the RNA-seq data, revealed that the two groups were
706 evidently distinguished for the first principal component (**Figure 2-figure supplement 1A**). Illumina
707 Stranded mRNA Prep was used to prepare cDNA libraries for RNA-Seq that was performed on an
708 Illumina Novaseq 6000 Sequencing system at IIT-Istituto Italiano di Tecnologia (Genova, Italy).
709 RNA-seq experiment produced an average of 26 million 150 nucleotide long paired-end reads per
710 sample. Dark cycles in sequencing from Novaseq 6000 machines can lead to a high quality stretches
711 of Guaninines artifacts; in order to remove these artifacts, low quality bases and N stretches from
712 reads were removed by Cutadapt software using "-u -U","--trim-n" and "—nextseq-trim=20"
713 parameters (Martin et al., 2011). Illumina adapter remotion were performed using Trimmomatic
714 software (Bolger et al., 2014). Reads whose length after trimming was <35 nt were discarded. Reads
715 were aligned to GRCm38 assembly using STAR aligner software (Dobin et al., 2013). Gene loci
716 fragment quantification was performed on Ensemble (release 87) gene annotation gtf using STAR –
717 quantMode GeneCounts parameter. Read counts of "reverse" configuration files were combined into
718 a count matrix file, which was given as input to edgeR (Robinson et al., 2010) R package for
719 differential expression analysis, after removing genes with less than 10 counts in at least two samples.
720 Samples were normalized using TMM. Model fitting and testing were performed using the glmFIT

721 and glmLRT functions. Gene-level FPKM values were calculated using rpkm function from the
722 edgeR package. FDR cutoff for selecting significant differentially expressed genes was set to 0.1.
723 Genes with less than 1 average FPKM in both conditions were filtered out. Heatmap of differentially
724 expressed genes was generated using heatmap3 R package (Zhao et al., 2014) from log2 transformed
725 FPKM values. Volcano plot were generated using "Enhanced Volcano" R package
726 (bioconductor.org/packages/release/bioc/vignettes/EnhancedVolcano/inst/doc/EnhancedVolcano).
727 Gene Ontology analyses were performed on up-regulated and down-regulated protein coding genes
728 using WebGestalt R package (Liao Y et al., 2019) applying Weighted Set Cover dimensionality
729 reduction.
730

731 **Cross-linking immunoprecipitation (CLIP) assay**

732 A total of 60 Charme^{WT} and 56 Charme^{KO} E15.5 embryonal hearts were collected, divided in two
733 distinct biological replicates and pestled for 2 min in PBS, 1x PIC and 1x PMSF. For each replicate,
734 the solution was filtered in a 70 µm strainer and the isolated cells were plated and UV-crosslinked
735 (4,000 µJ) in a Spectrolinker UV Crosslinker (Spectronics corporation). Upon harvesting, cells were
736 centrifuged 5 min at 600 x g and pellets resuspended in NP40 lysis buffer (50 mM HEPES pH 7.5,
737 150 mM KCl, 2 mM EDTA, 1 mM NaF, 0.5% (v/v) NP40, 0.5 mM DTT, 1x PIC,), incubated on ice
738 for 15 min and sonicated at low intensity six times with Bioruptor® Plus sonication device to ensure
739 nuclear membrane lysis. Lysate was diluted to a final concentration of 1 mg/ml. 30 µl of Dynabeads
740 Protein G magnetic particles (Thermo Fisher Scientific) per ml of total lysate were washed twice with
741 1 mL of PBS-Tween (0.02%), resuspended with 5 µg of MATR3 (Supplementary File 5) or IgG
742 antibodies (Immunoreagents Inc.) and incubated for 2 h at room temperature. Beads were then washed
743 twice with 1 mL of PBS-T and incubated with total extract overnight at 4°C. Beads were washed
744 three times with 1 mL of HighSalt NP40 wash buffer (50 mM HEPES-KOH, pH 7.5, 500 mM KCl,
745 0.05% (v/v) NP40, 0.5 mM DTT, 1x PIC) and resuspended in 100 µl of NP40 lysis buffer. For RNA

746 sequencing, 75 µl of the sample were treated for 30 min at 50°C with 1.2 mg/ml Proteinase K (Roche)
747 in Proteinase K Buffer (100 mM Tris-HCl, pH 7.5, 150mM NaCl, 12.5 mM EDTA, 2% (w/v) SDS).
748 For Western Blot analysis, 25 µl of the sample were heated at 95°C for 5 min and resuspended in 4x
749 Laemmli sample buffer (BioRad)/50 mM DTT before SDS-PAGE.
750

751 **MATR3 CLIP-seq analysis**

752 Trio RNA-Seq (Tecan Genomics, Redwood City, CA) has been used for library preparation following
753 the manufacturer's instructions. The sequencing reactions were performed on an Illumina Novaseq
754 6000 Sequencing system at IGA Technology services. CLIP-sequencing reactions produced an
755 average of 25 million 150 nucleotide long paired-end reads per sample Adaptor sequences and poor
756 quality bases were removed from raw reads using a combination of Trimmomatic version 0.39
757 (Bolger et al., 2014) and Cutadapt version 3.2 (Martin et al., 2011) softwares. Reads whose length
758 after trimming was <35 nt were discarded. Alignment to mouse GRCm38 genome and Ensembl
759 87 transcriptome was performed using STAR aligner version 2.7.7a (Dobin et al., 2013). Alignment
760 files were further processed by collapsing PCR duplicates using the MarkDuplicates tool included in
761 the Picard suite version 2.24.1 (http://broadinstitute.github.io/picard/) and discarding the multi-
762 mapped reads using BamTools version 2.5.1 (Barnett et al., 2011). Properly paired reads were
763 extracted using SAMtools version 1.7 (Li et al., 2009). GRCm38 genome was divided into 200 bp
764 long non-overlapping bins using the BEDtools makewindows tool (Quinlan et al., 2010). Properly
765 paired fragments falling in each bin were counted using the BEDtools intersect tool filtering out reads
766 mapping to rRNAs, tRNAs or mitochondrial genome in order to create sample-specific count files.
767 These files were given as input to Piranha version 1.2.1 (Uren et al., 2012) using *–x -s –u 0* parameters
768 to call significant bins for MATR3 Ip and IgG samples. BEDtools intersect was used to assign each
769 genomic bin to genes using Ensembl 87 annotation. For each gene the bin signal distribution in the
770 input sample was calculated after normalization of fragment counts by the total number of mapping

771 fragments. Ip significant bins presenting normalized signals lower than the upper-quartile value of
772 the related gene distribution were filtered out. After this filter, significant bins belonging to Ip samples
773 were merged using BEDTools merge tool. The number of fragments overlapping identified peaks and
774 the number overlapping the same genomic region in the Input sample were counted and used to
775 calculate fold enrichment (normalized by total mapping fragments counts in each data set), with
776 enrichment P-value calculated by Yates' Chi-Square test or Fisher Exact Test where the observed or
777 expected fragments number was below 5. Benjamini-Hochberg FDR procedure was applied for
778 multiple testing corrections. Peaks presenting log2 fold enrichment over Input >2 and FDR < 0.05 in
779 both Ip samples were selected as enriched regions (**Supplementary File 3).** BEDtools intersect tool
780 was used to annotate such regions based on their overlap with Ensembl 87 gene annotation and to
781 filter out transcripts hosting regions enriched in the IgG sample. Furthermore, htseq-count software
782 (Anders et al., 2015) with *-s no -m union -t gene* parameters was used to count reads from deduplicated
783 BAM files. Peaks overlapping transcripts with Input CPM (counts per million) > Ip CPM in both Ip
784 samples were filtered out. Gene Ontology analysis was performed on protein coding genes
785 overlapping enriched regions using WebGestalt R package (Liao et al., 2019). Bigwig of normalized
786 coverage (RPM, reads per million) files were produced using bamCoverage 3.5.1 from deepTools
787 tool set (http://deeptools.readthedocs.io/en/develop) on BAM files of uniquely mapping and
788 deduplicated reads using *--normalizeUsing CPM* parameter (Ramirez et al., 2014). Normalized
789 coverage tracks were visualized with IGV software (https://software.broadinstitute.org/software/igv/)
790 and Gviz R package (Hahne et al., 2016).
791 Local Motif Enrichment analysis was performed by using 10 nt-long sliding windows. For each
792 relative peak position/control set, the proportion of windows containing or not MATR3 motif was
793 calculated and tested for significant differences using two tails Fisher exact test. CLIP-seq IP signal
794 (FPM) relative to each position was retrieved from bigwig files using pyBigWig
795 (https://github.com/deeptools/pyBigWig). Motif Enrichment Analysis was performed using AME

796 software from MEME suite (Bailey et al., 2015) on a 100 nt window centred on the peak summit. For
797 each identified peak, a control set was by selecting 10 random regions from expressed (CPM>0) RNA
798 precursors. Differential analysis of MATR3 binding between Charme^{WT} and Charme^{KO} conditions
799 was assessed using DiffBind software (Ross-Innes et al., 2012).
800
801 **Protein analyses**
802 Protein extracts were prepared and analysed by western blot as in Desideri et al., 2020. See
803 **Supplementary File 5** for antibodies details.
804
805 **Single cell transcriptomics**
806 scRNAseq analysis was performed on publicly available datasets of E12.5 mouse hearts
807 (SRR10969391, Jackson-Weaver et al. 2020). FASTQ reads were aligned, filtered and counted
808 through the Cell Ranger pipeline (v4.0) using standard parameters. GRCm38 genome version was
809 used in alignment step and annotation refers to Ensembl Release87**.** The dataset was cleaned
810 (nFeature_RNA > 200 and < 6000, percent.mt > 0 and < 5, nCount_RNA > 500 and < 40000) and
811 cells were clustered using Seurat 4.0.5 (Stuart et al., 2019). Cluster uniformity was then checked using
812 COTAN (Galfrè et al., 2020) by evaluating if less than 1% of genes were over the threshold of 1.5 of
813 GDI. If a cluster resulted not uniform, with more than 1% of genes above 1.5, a new round of
814 clustering was performed. After this iterative procedure, the few remaining cells not fitting any
815 cluster, were discarded. A dataset of 4014 cells and 34 clusters was obtained. COTAN function
816 *clustersDeltaExpression* (github devel branch) was used to obtain a correlation coefficient and a *p*-
817 value for each gene and each cluster. From the correlation matrix, a cosine dissimilarity between
818 clusters was estimated and used to plot a dendrogram (with the ward.D2 algorithm, **Figure 1-figure**
819 **supplement 1D**). The tree was used to decide which clusters could be merged. Cell type for each
820 final cluster was assigned based on a list of markers (Jackson-Weaver et al., 2020; Li et al., 2016) as

821 follows. Cardiomyocytes (1834 cells): Myh6+, Nppa+, Atrial CM (333 cells): are also Myl1+, Myl4+
822 , Ventricular CM (1289): are also Myl2+, Myl3+, interventricular septum CM (117 cells): are also
823 TBX20+, Gja5+ (Franco et al., 2006), Venous Pole CM (95 cells): also Osr1+ (Meilhac et al., 2018),
824 Outflow Tract CM (72 cells): also Isl1+, Sema3c+, Neural crest cells (there are two clusters
825 expressing their markers: 1.NC with 48 cells and 2.NC with 68 cells): Msx1+, Twist1+, Sox9+,
826 Epicardial cells (359 cells): Cebpb+, Krt18+, Fibroblasts like cells (278 cells): Tcf21+, Fn1+,
827 Endothelial cells (168 cells): Klf2+, Pecam1+, Cdh5+, Smooth muscle cells (710 cells): Cnn1+,
828 Acta2+, Tagln2+, Tagln+, Hemopoietic myeloid cells (79 cells): Fcer1g+, Hemopoietic red blood
829 cells (397 cells): Hba-a1+. The final UMAP plot with the cell assignment is shown in **Figure 1-figure**
830 **supplement 1E**. Heatmap in **Figure 1-figure supplement 1F** shows a coherent assignment between
831 final clusters and cell type with additional marker genes. For correlation analyses (**Figure 1G**),
832 relevant genes in each subpopulation of interest (CM-VP, CM-OFT, A-CM, CM-IVS, V-CM) were
833 analysed separately by applying COTAN on a test dataset composed by the subpopulation in exam,
834 together with a fixed contrasting cell group with the SM and EC cells (see **Figure 1E**).
835

836 **Echocardiography**

837 The echocardiographer was blinded to the phenotypes. Mice were anaesthetised with 2.5% Avertin
838 (Sigma T48402) to perform echocardiographic structural (measurement of left ventricular diameters
839 and wall thickness) and functional (fractional shortening) analyses with a VEVO 3100 (Visualsonics)
840 using a mx550d probe. We used avertin since it does not induce significant cardiodepressant effects,
841 potentially affecting our echocardiographic experiments compared to ketamine combinations, such
842 as ketamine+xylazine. The fractional shortening (FS) of the left ventricle was calculated as FS% =
843 (left ventricular end-diastolic diameter (LVEDD)-left ventricular end-systolic diameter
844 (LVESD)/LVEDD) x 100, representing the relative change of the left ventricular diameters during

845 the cardiac cycle. The mean FS of the left ventricle was determined by the average of FS
846 measurements of the left ventricular contraction over 3 beats.
847
848 **Data accessibility**
849 The data presented in this study will be openly available in NCBI Gene Expression Omnibus (GEO)
850 database (https://www.ncbi.nlm.nih.gov/geo/), reference number GSE200878 for RNA-seq data and
851 GSE200877 for MATR3 CLIP-seq data.
852
853 **Statistical methods and rigour**
854 Statistical tests, p-values, and n for each analysis are reported in the corresponding figure legend. For
855 each experiment, at least three individual animals or pools of littermates were used (see each figure
856 legend for details). No sex bias was introduced by randomly choosing among male and female mice.
857 All analyses were performed by 1 or more blinded investigators.
858
859 **Competing interest**
860 The authors declare no competing interests.
861
862 **Acknowledgments**
863 The authors acknowledge Pietro Laneve, Francesca Pagano, Andrea Cipriano and Marco D'Onghia
864 for helpful discussion, Alessandro Calicchio for cloning the probe templates for *in-situ* hybridization
865 analyses and Marcella Marchioni for technical help. This work was supported by grants from
866 Sapienza University (prot. RM11916B7A39DCE5 and RM12117A5DE7A45B), POR FESR Lazio
867 2020-T0002E0001 and MUR PNRR "National Center for Gene Therapy and Drugs based on RNA
868 Technology" (Project no. CN3221842F1B2436 CN3_Spoke 3) to MB.
869

870 **REFERENCES**

871 Akerberg BN, Gu F, VanDusen NJ, Zhang X, Dong R, Li K, Zhang B, Zhou B, Sethi I, Ma Q, et al. 2019. A
872 reference map of murine cardiac transcription factor chromatin occupancy identifies dynamic and conserved
873 enhancers. *Nat Commun* **10**: 4907.

874 Ajima R, Akazawa H, Kodama M, Takeshita F, Otsuka A, Kohno T, Komuro I, Ochiya T, Yokota J. 2008.
875 Deficiency of Myo18B in mice results in embryonic lethality with cardiac myofibrillar aberrations. *Genes*
876 *Cells* **13**:987-99.
877
878 Anders S, Pyl PT, Huber W. 2015. HTSeq--a Python framework to work with high-throughput sequencing
879 data. *Bioinformatics* **31**:166-169.

880 Anderson K, Anderson D, McAnally J, Shelton JM, Bassel-Duby R, Olson EN. 2016. Transcription of the
881 non-coding RNA upperhand controls Hand2 expression and heart development. *Nature* **539**: 433–436.

882 Anderson DM, Anderson KM, Nelson BR, McAnally JR, Bezprozvannaya S, Shelton JM, Bassel-Duby R, &
883 Olson EN. 2021. A myocardin-adjacent lncRNA balances SRF-dependent gene transcription in the heart.
884 *Genes & development* **35**: 835–840.

885 Ang YS, Rivas RN, Ribeiro A, Srivas R, Rivera J, Stone NR, Pratt K, Mohamed T, Fu JD, Spencer CI, et al.
886 2016. Disease Model of GATA4 Mutation Reveals Transcription Factor Cooperativity in Human
887 Cardiogenesis. *Cell* **167**: 1734–1749.

888 Aydin B, Kakumanu A, Rossillo M, Moreno-Estellés M, Garipler G, Ringstad N, Flames N, Mahony S, &
889 Mazzoni EO. 2019. Proneural factors Ascl1 and Neurog2 contribute to neuronal subtype identities by
890 establishing distinct chromatin landscapes. *Nature Neuroscience* **22**: 897.

891 Azad FM, Polignano LI, Proserpio V, Oliviero S. 2021. Long Noncoding RNAs in Human Stemness and
892 Differentiation. *Trends in Cell Biology* **31**: 542-545.

893 Bailey TL, Johnson J, Grant CE, Noble WS. 2015. The MEME Suite. *Nucleic Acids Res*. **43**(W1):W39-49.

894 Ballarino M, Cazzella V, D'Andrea D, Grassi L, Bisceglie L, Cipriano A, Santini T, Pinnarò C, Morlando M,
895 Tramontano A, Bozzoni I. 2015. Novel Long Noncoding RNAs (lncRNAs) in Myogenesis: a miR-31
896 Overlapping lncRNA Transcript Controls Myoblast Differentiation. *Molecular and Cellular Biology*, **35**: 728–
897 736.

898 Ballarino M, Cipriano A, Tita R, Santini T, Desideri F, Morlando M, Colantoni A, Carrieri C, Nicoletti C,
899 Musarò A, Carroll DO, Bozzoni I. 2018. Deficiency in the nuclear long noncoding RNA Charme causes
900 myogenic defects and heart remodeling in mice. *The EMBO Journal* **37**: e99697.

901 Banerjee A, Vest KE, Pavlath GK, Corbett AH. 2017. Nuclear poly(A) binding protein 1 (PABPN1) and
902 Matrin3 interact in muscle cells and regulate RNA processing. *Nucleic Acids Research* **45**: 10706–10725.

903 Barnett DW, Garrison EK, Quinlan AR, Strömberg MP, Marth GT. 2011. BamTools: a C++ API and toolkit
904 for analyzing and managing BAM files. *Bioinformatics* **27**:1691-2.

905 Bhat P, Honson D, Guttman M. 2021. Nuclear compartmentalization as a mechanism of quantitative control
906 of gene expression. *Nat Rev Mol Cell Biol* **22**:653-670.

907 Bolger AM, Lohse M, Usadel B. 2014. Trimmomatic: A flexible trimmer for Illumina sequence data.
908 *Bioinformatics* **30**: 2114–2120.

909 Bouveret R, Waardenberg AJ, Schonrock N, Ramialison M, Doan T, de Jong D, Bondue A, Kaur G, Mohamed
910 S, Fonoudi H, et al. 2015. NKX2-5 mutations causative for congenital heart disease retain functionality and
911 are directed to hundreds of targets. *eLife* **4***:* e06942.

912 Bruneau BG. 2013. Signaling and transcriptional networks in heart development and regeneration. *Cold Spring*
913 *Harbor perspectives in biology* **5**: a008292.

914 Buckingham M. 2017. Gene regulatory networks and cell lineages that underlie the formation of skeletal
915 muscle. *PNAS* **114**: 5830-5837.

916 Buonaiuto G, Desideri F, Taliani V, Ballarino M. 2021. Muscle Regeneration and RNA: New Perspectives for
917 Ancient Molecules. *Cells* 10: 2512.

918 Castro-Mondragon JA, Riudavets-Puig R, Rauluseviciute I, Lemma RB, Turchi L, Blanc-Mathieu R, Lucas J,
919 Boddie P, Khan A, Manosalva Pérez N et al. JASPAR 2022: the 9th release of the open-access database of
920 transcription factor binding profiles. Nucleic Acids Res. 2022 Jan 7;50(D1):D165-D173. doi:
921 10.1093/nar/gkab1113. PMID: 34850907; PMCID: PMC8728201.

922 Cazzella V, Martone J, Pinnarò C, Santini T, Twayana SS, Sthandier O, D'Amico A, Ricotti V, Bertini E,
923 Muntoni F, Bozzoni I. 2012. Exon 45 skipping through U1-snRNA antisense molecules recovers the Dys-
924 nNOS pathway and muscle differentiation in human DMD myoblasts. *Mol Ther.* **20**: 2134-42.

925 Center for Disease Control and Prevention, (2020, December 9). Data and Statistics on Congenital Heart
926 Defects. https://www.cdc.gov/ncbddd/heartdefects/data.html

927 Cha HJ, Uyan Ö, Kai Y, Liu T, Zhu Q, Tothova Z, Botten GA, Xu J, Yuan GC, Dekker J, Orkin SH. 2021.
928 Inner nuclear protein Matrin-3 coordinates cell differentiation by stabilizing chromatin architecture. *Nat*
929 *Commun*. **12**: 6241.

930 Choquet C, Kelly RG, & Miquerol L. 2019. Defects in Trabecular Development Contribute to Left Ventricular
931 Noncompaction. *Pediatric Cardiology* **40**: 1331–1338.

932 Chu H, Kohane DS, & Langer R. 2016. RNA therapeutics - The potential treatment for myocardial infarction.
933 *Regenerative Therapy* **4**: 83–91.

934 Cipriano A, Ballarino M. 2018. The Ever-Evolving Concept of the Gene: The Use of RNA/Protein
935 Experimental Techniques to Understand Genome Functions. *Front Mol Biosci* **6**: 5-20.

936 Coelho MB, Attig J, Ule J, Smith CW. 2016. Matrin3: connecting gene expression with the nuclear matrix.
937 *Wiley Interdiscip Rev RNA* **7**: 303-15.

938 D'Ambra E, Santini T, Vitiello E, D'Uva S, Silenzi V, Morlando M, Bozzoni I. 2021. Circ-Hdgfrp3 shuttles
939 along neurites and is trapped in aggregates formed by ALS-associated mutant FUS. *iScience* **24**: 103504.

940 D'Antonio M, Nguyen JP, Arthur TD, Matsui H, Donovan MKR, D'Antonio-Chronowska A, Frazer KA. 2022.
941 In heart failure reactivation of RNA-binding proteins is associated with the expression of 1,523 fetal-specific
942 isoforms. *PLoS computational biology* **18**: e1009918.

943 DeLaughter DM, Bick AG, Wakimoto H, McKean D, Gorham JM, Kathiriya IS, Hinson JT, Homsy J, Gray J,
944 Pu W, et al. 2016. Single-Cell Resolution of Temporal Gene Expression during Heart Development. *Dev Cell*
945 **39**:480-490.

946 Desideri F, Cipriano A, Petrezselyova S, Buonaiuto G, Santini T, Kasparek P, Prochazka J, Janson, G, Paiardini
947 A, et al. 2020. Intronic Determinants Coordinate Charme lncRNA Nuclear Activity through the Interaction
948 with MATR3 and PTBP1. *Cell Reports* **33**: 108548.

949 de Soysa TY, Ranade SS, Okawa S, et al. 2019 Single-cell analysis of cardiogenesis reveals basis for organ-
950 level developmental defects. *Nature* **572**: 120-124.

951 Dobin A, Davis CA, Schlesinger F, Drenkow J, Zaleski C, Jha S, Batut P, Chaisson M, Gingeras TR. 2013.
952 STAR: ultrafast universal RNA-seq aligner. *Bioinformatics* **29**:15-21.

Dunn NR, Vincent SD, Oxburgh L, Robertson EJ, Bikoff EK. 2004. Combinatorial activities of Smad2 and Smad3 regulate mesoderm formation and patterning in the mouse embryo. *Development* **131**: 1717-28.

England J, Loughna S. 2013. Heavy and light roles: myosin in the morphogenesis of the heart. *Cell Mol Life Sci*. **70**:1221-39.

Feit H, Silbergleit A, Schneider LB, Gutierrez JA, Fitoussi RP, Réyès C, Rouleau GA, Brais B, Jackson CE, Beckmann JS, Seboun E. 1998. Vocal cord and pharyngeal weakness with autosomal dominant distal myopathy: clinical description and gene localization to 5q31. *Am J Hum Genet.* **63**:1732-42.

Franco D, Meilhac SM, Christoffels VM, Kispert A, Buckingham M, Kelly RG. 2006. Left and right ventricular contributions to the formation of the interventricular septum in the mouse heart. *Dev Biol*. **294**: 366-375.

Galfrè SG, Morandin F, Pietrosanto M, Cremisi F, Helmer-Citterich M. 2020. COTAN: scRNA-seq data analysis based on gene co-expression, *NAR Genomics and Bioinformatics* 3: lqab072.

García-Padilla C, Aránega A, Franco D. 2018. The role of long non-coding RNAs in cardiac development and disease. *AIMS Genet* **5**: 124-140.

Goonasekera SA, Hammer K, Auger-Messier M, Bodi I, Chen X, Zhang H, Reiken S, Elrod JW, Correll RN, York AJ, et al. 2012. Decreased cardiac L-type Ca^{2+} channel activity induces hypertrophy and heart failure in mice. *J Clin Invest* **122**: 280-290.

Grote P, Wittler L, Hendrix D, Koch F, Währisch S, Beisaw A, Macura K, Bläss G, Kellis M, Werber M, et al. 2013. The tissue-specific lncRNA Fendrr is an essential regulator of heart and body wall development in the mouse. *Dev Cell* **24**:206-214.

Hahne F, Ivanek R. 2016. Visualizing Genomic Data Using Gviz and Bioconductor. *Methods Mol Biol* **18**: 335-51.

Hall JM, Kainth AS, Rowton MJ, Lu E, Haddad G, Keplinger AJ, Šćepanović J, Perez-Cervantes S, Chan SSK, Piccirilli JA, et al. 2021.The cardiac lncRNA Chantico directly regulates *Cxcl1* chemokine transcription. *bioRxiv* doi: 10.1101/2021.12.23.474040.

Han P, Li W, Lin CH, Yang J, Shang C, Nurnberg ST, Jin KK, Xu W, Lin CY, Lin CJ, et al. 2014. A long noncoding RNA protects the heart from pathological hypertrophy. *Nature* **514**: 102–106.

Han X, Zhang J, Liu X, Fan X, Ai S, Luo Y, Li X, Jin H, Luo S, Zheng H, et al. 2019. The lncRNA Hand2os1/Uph locus orchestrates heart development through regulation of precise expression of Hand2. *Development* **146**: dev176198.

Hazra R, Brine L, Garcia L, Benz B, Chirathivat N, Shen MM, Wilkinson JE, Lyons SK, Spector DL. 2022. Platr4 is an early embryonic lncRNA that exerts its function downstream on cardiogenic mesodermal lineage commitment. *Developmental cell* **57**: 2450–2468.e7.

Higaki T, Akita K, Katoh K. 2020. Coefficient of variation as an image-intensity metric for cytoskeleton bundling. *Scientific Reports* **10**:22187.

Horsthuis T, Houweling AC, Habets PE. MH, De Lange FJ, El Azzouzi H, Clout DEW, Moorman AFM, Christoffels VM. 2008. Distinct regulation of developmental and heart disease-induced atrial natriuretic factor expression by two separate distal sequences. *Circulation Research* **102**: 849–859.

Hu G, Niu F, Humburg BA, Liao K, Bendi S, Callen S, Fox HS, Buch S. 2018. Molecular mechanisms of long noncoding RNAs and their role in disease pathogenesis. *Oncotarget* 9: 18648–18663.

994 Ikeda S, Mizushima W, Sciarretta S, Abdellatif M, Zhai P, Mukai R, Fefelova N, Oka SI, Nakamura M, Del
995 Re DP, et al. 2019. Hippo Deficiency Leads to Cardiac Dysfunction Accompanied by Cardiomyocyte
996 Dedifferentiation During Pressure Overload. *Circ Res.* **124**: 292-305.

997 Jackson-Weaver O, Ungvijanpunya N, Yuan Y, Qian J, Gou Y, Wu J, Shen H, Chen Y, Li M, et al. 2020.
998 PRMT1-p53 Pathway Controls Epicardial EMT and Invasion. *Cell Rep* **31**:107739.

999 Jusic A, Thomas PB, Wettinger SB, Dogan S, Farrugia R, Gaetano C, Tuna BG, Pinet F, Robinson EL, Tual-
1000 Chalot S, Stellos K, Devaux Y. 2022. EU-CardioRNA COST Action CA17129. Noncoding RNAs in age-
1001 related cardiovascular diseases. *Ageing Res Rev*. **77**:101610.

1002 Kattman SJ, Witty AD, Gagliardi M, Dubois NC, Niapour M, Hotta A, Ellis J, Keller G. 2011. Stage-specific
1003 optimization of activin/nodal and BMP signaling promotes cardiac differentiation of mouse and human
1004 pluripotent stem cell lines. *Cell Stem Cell*. **8**:228-40.

1005 Kim NJ, Lee KH, Son Y, Nam AR, Moon EH, Pyun JH, Park J, Kang JS, Lee YJ, Cho JY. 2021.
1006 Spatiotemporal expression of long noncoding RNA Moshe modulates heart cell lineage commitment. *RNA*
1007 *Biol*. **18**: 640-654.

1008 Klattenhoff CA, Scheuermann JC, Surface LE, Bradley RK, Fields PA, Steinhauser ML, Ding H, Butty VL,
1009 Torrey L, Haas S et al., 2013. Braveheart, a long noncoding RNA required for cardiovascular lineage
1010 commitment. *Cell* **152**: 570–583.

1011 Kodo K, Nishizawa T, Furutani M, Arai S, Yamamura E, Joo K, Takahashi T, Matsuoka R, Yamagishi H.
1012 2009. GATA6 mutations cause human cardiac outflow tract defects by disrupting semaphorin-plexin signaling.
1013 *Proceedings of the National Academy of Sciences of the United States of America* **106**: 13933–13938.

1014 Latham SL, Weiß N, Schwanke K, Thiel C, Croucher DR, Zweigerdt R, Manstein DJ, Taft MH. 2020. Myosin-
1015 18B Regulates Higher-Order Organization of the Cardiac Sarcomere through Thin Filament Cross-Linking
1016 and Thick Filament Dynamics. *Cell Rep* **32**: 108090.

1017 Li G, Xu A, Sim S, Priest JR, Tian X, Khan T, Quertermous T, Zhou B, Tsao PS, Quake SR, et al. 2016.
1018 Transcriptomic Profiling Maps Anatomically Patterned Subpopulations among Single Embryonic Cardiac
1019 Cells. *Dev Cell* **39**:491-507.

1020 Li H, Handsaker B, Wysoker A, Fennell T, Ruan J, Homer N, Marth G, Abecasis G, Durbin R. 2009.1000
1021 Genome Project Data Processing Subgroup. The Sequence Alignment/Map format and SAMtools.
1022 *Bioinformatics* **25**: 2078-2079.

1023 Liao Y, Wang J, Jaehnig EJ, Shi Z, Zhang B. 2019. WebGestalt 2019: gene set analysis toolkit with revamped
1024 UIs and APIs. *Nucleic Acids Res*. **47**:W199-W205.

1025 Luna-Zurita L, Stirnimann CU, Glatt S, Kaynak BL, Thomas S, Baudin F, Samee MAH, He D, Small EM,
1026 Mileikovsky M, et al. 2016. Complex Interdependence Regulates Heterotypic Transcription Factor
1027 Distribution and Coordinates Cardiogenesis. *Cell* **164**: 999–1014.

1028 MacGrogan D, Münch J, de la Pompa JL. 2018. Notch and interacting signalling pathways in cardiac
1029 development, disease, and regeneration. *Nat Rev Cardiol.* **15**: 685-704.

1030 Malik AM, Miguez RA, Li X, Ho YS, Feldman EL, Barmada SJ. 2018. Matrin 3-dependent neurotoxicity is
1031 modified by nucleic acid binding and nucleocytoplasmic localization. *Elife* **17**;7:e35977.

1032 Martin M. 2011. Cutadapt removes adapter sequences from high-throughput sequencing reads.
1033 *EMBnet.journal* **17**: 10-12.

1034 Mattick J. 2004. RNA regulation: a new genetics?. *Nat Rev Genet* **5**: 316–323.

1035 Meilhac SM, Buckingham ME. 2018. The deployment of cell lineages that form the mammalian heart. *Nat*
1036 *Rev Cardiol* **15**:705-724.

1037 Morton SU, Quiat D, Seidman, JG, Seidman C E. 2022. Genomic frontiers in congenital heart disease. *Nature*
1038 *reviews. Cardiology* **19**: 26–42.

1039 Moorman AF, Christoffels VM. 2003.Cardiac chamber formation: development, genes, and evolution. *Physiol*
1040 *Rev* **83**: 1223-67.

1041 Nadadur RD, Broman MT, Boukens B, Mazurek SR, Yang X, van den Boogaard M, Bekeny J, Gadek M,
1042 Ward T, Zhang M, et al. 2016. Pitx2 modulates a Tbx5-dependent gene regulatory network to maintain atrial
1043 rhythm. *Science translational medicine* **8**: 354ra115.

1044 Noguchi S, Arakawa T, Fukuda S, Furuno M, Hasegawa A, Hori F, Ishikawa-Kato S, Kaida K, Kaiho A,
1045 Kanamori-Katayama M, et al. 2017. FANTOM5 CAGE profiles of human and mouse samples. *Scientific Data*
1046 **4**: 1–10.

1047 Olson E. 1993. Regulation of muscle transcription by the MyoD family. The heart of the matter. *Circulation*
1048 *research* **72**: 1-6.

1049 Ounzain S, Micheletti R, Arnan C, Plaisance I, Cecchi D, Schroen B, Reverter F, Alexanian M, Gonzales C,
1050 Ng, SY, Bussotti G et al., 2015. CARMEN, a human super enhancer-associated long noncoding RNA
1051 controlling cardiac specification, differentiation and homeostasis. *Journal of molecular and cellular*
1052 *cardiology* **89**: 98–112.

1053 Padula SL, Velayutham N, Yutzey KE. 2021. Transcriptional Regulation of Postnatal Cardiomyocyte
1054 Maturation and Regeneration. *Int J Mol Sci*. **22**(6):3288.

1055 Pagano F, Calicchio A, Picchio V, Ballarino M. 2020. The Noncoding Side of Cardiac Differentiation and
1056 Regeneration. *Current Stem Cell Research & Therapy* **15**: 723–738.

1057 Pinheiro A, Naya FJ. 2021. The Key Lnc (RNA)s in Cardiac and Skeletal Muscle Development, Regeneration,
1058 and Disease. *Journal of Cardiovascular Development and Disease* **8**: 84.

1059 Ponnusamy M, Liu F, Zhang YH, Li RB, Zhai M, Liu F, Zhou LY, Liu CY, Yan KW, Dong YH, et al. 2019.
1060 Long Noncoding RNA CPR (Cardiomyocyte Proliferation Regulator) Regulates Cardiomyocyte Proliferation
1061 and Cardiac Repair. *Circulation* **139**: 2668–2684.

1062 Quinlan AR, Hall IM. 2010. BEDTools: a flexible suite of utilities for comparing genomic features.
1063 *Bioinformatics* **26**: 841-842.

1064 Quintero-Rivera F, Xi QJ, Keppler-Noreuil KM, Lee JH, Higgins AW, Anchan RM, Roberts AE, Seong IS,
1065 Fan X, Lage K, et al. 2015. MATR3 disruption in human and mouse associated with bicuspid aortic valve,
1066 aortic coarctation and patent ductus arteriosus. *Human molecular genetics* **24**: 2375–2389.

1067 Ramesh N, Kour S, Anderson EN, Rajasundaram D, Pandey UB. 2020. RNA-recognition motif in Matrin-3
1068 mediates neurodegeneration through interaction with hnRNPM. *Acta neuropathol commun* **8**, 138.

1069 Ramírez F, Dündar F, Diehl S, Grüning BA, Manke T. 2014. deepTools: a flexible platform for exploring
1070 deep-sequencing data. *Nucleic Acids Res* **42**: W187-91.

1071 Ray D, Kazan H, Cook KB, Weirauch MT, Najafabadi HS, Li X, Gueroussov S, Albu M, Zheng H, Yang A,
1072 et al. 2013, A compendium of RNA-binding motifs for decoding gene regulation. Nature 499: 172–177.

1073 Ribeiro DM, Zanzoni A, Cipriano A, Delli Ponti R, Spinelli L, Ballarino M, Bozzoni I, Tartaglia GG, Brun C.
1074 2018. Protein complex scaffolding predicted as a prevalent function of long non-coding RNAs. *Nucleic Acids*
1075 *Research* **46**: 917–928.

1076 Rinn JL, Chang HY. 2012. Genome regulation by long noncoding RNAs. *Annual review of biochemistry* **81**:
1077 145–166.

1078 Ritter N, Ali T, Kopitchinski N, Schuster P, Beisaw A, Hendrix DA, Schulz MH, Müller-McNicoll M,
1079 Dimmeler S, Grote P. 2019. The lncRNA Locus Handsdown Regulates Cardiac Gene Programs and Is
1080 Essential for Early Mouse Development. *Dev Cell*. **50**:644-657.

1081 Riva P, Ratti A, Venturin M. 2016. The Long Non-Coding RNAs in Neurodegenerative Diseases: Novel
1082 Mechanisms of Pathogenesis. *Current Alzheimer research* **13**: 1219–1231.

1083 Robinson MD, McCarthy DJ, Smyth GK. 2010. edgeR: a Bioconductor package for differential expression
1084 analysis of digital gene expression data. *Bioinformatics* **26**:139-40.

1085 Roden C, Gladfelter AS. 2021. RNA contributions to the form and function of biomolecular condensates. *Nat*
1086 *Rev Mol Cell Biol* **22**:183-195.

1087 Ross-Innes CS, Stark R, Teschendorff AE, Holmes KA, Ali HR, Dunning MJ, Brown GD, Gojis O, Ellis IO,
1088 Green AR, etal.,. 2012. Differential oestrogen receptor binding is associated with clinical outcome in breast
1089 cancer. *Nature* **481**.

1090 Samsa LA, Yang B, & Liu J. 2013. Embryonic cardiac chamber maturation: Trabeculation, conduction, and
1091 cardiomyocyte proliferation. *American Journal of Medical Genetics, Part C: Seminars in Medical Genetics*
1092 **163**: 157–168.
1093
1094 Scheuermann JC, Boyer LA. 2013. Getting to the heart of the matter: long non-coding RNAs in cardiac
1095 development and disease. *EMBO J* **32**: 1805-16.
1096
1097 Schneider CA, Rasband WS. Eliceiri KW, 2012. NIH Image to ImageJ: 25 years of image analysis. *Nat.*
1098 *Methods* **9** 671–675,
1099
1100 Senderek J, Garvey SM, Krieger M, Guergueltcheva V, Urtizberea A, Roos A, Elbracht M, Stendel C, Tournev
1101 I, Mihailova V, et al.,. 2009. Autosomal-dominant distal myopathy associated with a recurrent missense
1102 mutation in the gene encoding the nuclear matrix protein, matrin 3. *Am J Hum Genet.* **84**:511-8.
1103
1104 Srivastava D. 2006. Genetic regulation of cardiogenesis and congenital heart disease. *Annual review of*
1105 *pathology* **1**: 199–213.

1106 Sprunger ML, Lee K, Sohn BS, Jackrel ME. 2022. Molecular determinants and modifiers of Matrin-3
1107 toxicity, condensate dynamics, and droplet morphology. *iScience* **25**:103900.
1108
1109 Steimle JD, Moskowitz IP. 2017. TBX5: A Key Regulator of Heart Development. *Current topics in*
1110 *developmental biology*, **122:** 195–221.

1111 Stuart T, Butler A, Hoffman P, Hafemeister C, Papalexi E, Mauck WM 3rd, Hao Y, Stoeckius M, Smibert P,
1112 Satija R. 2019. Comprehensive Integration of Single-Cell Data. *Cell* **177**:1888-1902.

1113 Tao YK, Zeng H, Zhang GQ, Chen ST, Xie XJ, He X, Wang S, Wen H, Chen JX. 2017. Notch3 deficiency
1114 impairs coronary microvascular maturation and reduces cardiac recovery after myocardial ischemia. *Int J*
1115 *Cardiol* **236**:413-422.
1116
1117 Tian X, Li Y, He L, Zhang H, Huang X, Liu Q, Pu W, Zhang L, Li Y, Zhao H, et al., 2017. Identification of a
1118 hybrid myocardial zone in the mammalian heart after birth. *Nat Commun*. **20**:8(1):87

1119 Uemura Y, Oshima T, Yamamoto M, Reyes CJ, Costa Cruz PH, Shibuya T, & Kawahara Y. 2017. Matrin3
1120 binds directly to intronic pyrimidine-rich sequences and controls alternative splicing. *Genes to cells : devoted*
1121 *to molecular & cellular mechanisms* **22**: 785–798.

1122 Ulitsky I, Bartel DP. 2013. lincRNAs: genomics, evolution, and mechanisms. *Cell* **154**: 26–46.

1123 Uosaki H, Cahan P, Lee DI, Wang S, Miyamoto M, Fernandez L, Kass DA, Kwon C. 2015. Transcriptional
1124 landscape of cardiomyocyte maturation. *Cell Rep* **13**:1705–1716.

1125 Uren PJ, Bahrami-Samani E, Burns SC, Qiao M, Karginov FV, Hodges E, Hannon GJ, Sanford JR, Penalva
1126 LOF, Smith AD. 2012. Site identification in high-throughput RNA–protein interaction data. *Bioinformatics*
1127 **28**: 3013–3020.

1128 van den Hoogenhof MMG, Beqqali A, Amin AS, van der Made I, Aufiero S, Khan MAF, Schumacher CA,
1129 Jansweijer JA, van Spaendonck-Zwarts KY, Remme CA, et al. 2018. RBM20 Mutations Induce an
1130 Arrhythmogenic Dilated Cardiomyopathy Related to Disturbed Calcium Handling. *Circulation* **138**: 1330-
1131 1342.

1132 Wang K, Holt C, Lu J, Brohus M, Larsen KT, Overgaard MT, Wimmer R, Van Petegem F. 2018. Arrhythmia
1133 mutations in calmodulin cause conformational changes that affect interactions with the cardiac voltage-gated
1134 calcium channel. *Proc Natl Acad Sci U S A* **115**: E10556-E10565.

1135 Wang Y, Chen J, Cowan DB, Wang DZ. 2021. Non-coding RNAs in cardiac regeneration: Mechanism of
1136 action and therapeutic potential. *Seminars in cell & developmental biology* **118**: 150–162.

1137 Wang Z, Zhang XJ, Ji YX, Zhang P, Deng KQ, Gong J, Ren S, Wang X, Chen I, Wang I, et al. 2016. The long
1138 noncoding RNA Chaer defines an epigenetic checkpoint in cardiac hypertrophy. *Nat. Med.* **22**: 1131–1139.

1139 Yang XH, Nadadur RD, Hilvering CR, Bianchi V, Werner M, Mazurek SR, Gadek M, Shen KM, Goldman
1140 JA, Tyan L et al. 2017. Transcription-factor-dependent enhancer transcription defines a gene regulatory
1141 network for cardiac rhythm. *Elife* **6**: e31683.

1142 Yao RW, Wang Y, Chen LL. 2019. Cellular functions of long noncoding RNAs. *Nature cell biology* **21**: 542–
1143 551.

1144 Zhao S, Guo Y, Sheng Q, Shyr Y. 2014. Advanced heat map and clustering analysis using heatmap3. *Biomed.*
1145 *Res. Int* e986048.

1146 Zimmerman MS, Carswell Smith AG, Sable CA, Echko MM, Wilner LB, Olsen HE, Tasew Atalay H, Awasthi
1147 A, Bhutta ZA, Boucher JL, et al. 2020. Global, regional, and national burden of congenital heart disease, 1990–
1148 2017: a systematic analysis for the Global Burden of Disease Study 2017. *The Lancet. Child & adolescent*
1149 *health* **4**: 185–200.

Figure 1-figure supplement 1

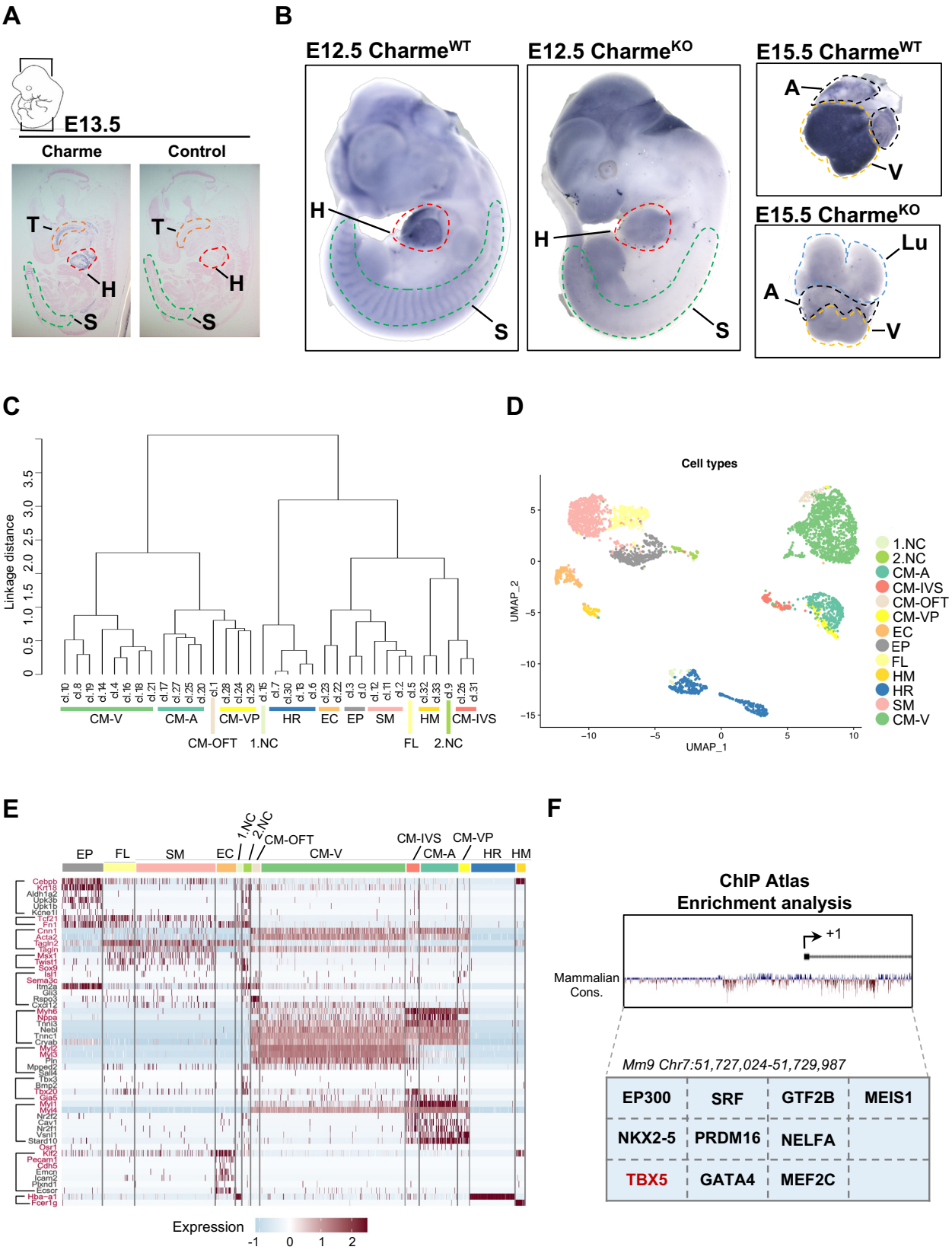

Figure 1-Figure supplement 1. Related to Figure 1

1152 **A)** *In-situ* hybridization (ISH) performed on E13.5 embryonal cryo-sections using digoxigenin-
1153 labelled RNA antisense (Charme, left panel) or sense (control, right panel) probes against Charme.
1154 T: Tongue (orange); H: Heart (red); S: Somites (green).
1155 **B)** Whole-mount *in-situ* hybridization (WISH) performed on Charme^{WT} and Charme^{KO} intact embryos
1156 (E12.5, left panels) and hearts (E15.5, right panels). Signal is specifically detected in heart (H, red
1157 line) and somites (S, green line). The specificity of the staining can be appreciated by the complete
1158 absence of signals in the Charme^{KO} samples. Heart (H, red line); Somites (S, green line); A: Atria
1159 (black line); V: Ventricles (yellow line).
1160 **C)** Dendrogram showing the relationships between homogeneous clusters. All the informative
1161 transcriptome was used to create a hierarchical clustering between homogeneous cell clusters.
1162 Colored lines mark which clusters were merged for the final clustering (Figure 1-Figure supplement
1163 1D-E). CM: Cardiomyocytes, A-CM: Atrial-CM, V-CM: Ventricular-CM, ISV: Interventricular
1164 Septum, VP: Venous Pole, OFT: Outflow Tract, NC: Neural Crest cell, EP: Epicardial cells, FL:
1165 Fibroblasts like cells, EC: Endothelial Cells, SM: Smooth Muscle cells, HM: Hemopoietic Myeloid
1166 cells, HR: Hemopoietic Red blood cells.
1167 D) Seurat (Stuart et al., 2019) UMAP plot coloured by final cell assignments. See Materials and
1168 Methods for details.
1169 **E)** Heatmap was generated by Seurat DoHeatmap (Stuart et al., 2019) and represents, for each cell of
1170 the identified sub-populations, the log normalized expression of cell identity markers (listed on the
1171 left). Genes used for cell clustering are marked in red. Maximum expression value (red), minimum
1172 expression value (light blue). Correspondence between gene markers and cell types is indicated on
1173 the left.
1174 **F)** *In silico* analysis of cardiovascular TF binding sites on Charme promoter using the enrichment
1175 analysis tool on the ChIP Atlas database (https://chip-atlas.org/enrichment_analysis) by setting the
1176 threshold at 200.

1177

Figure 2-figure supplement 1

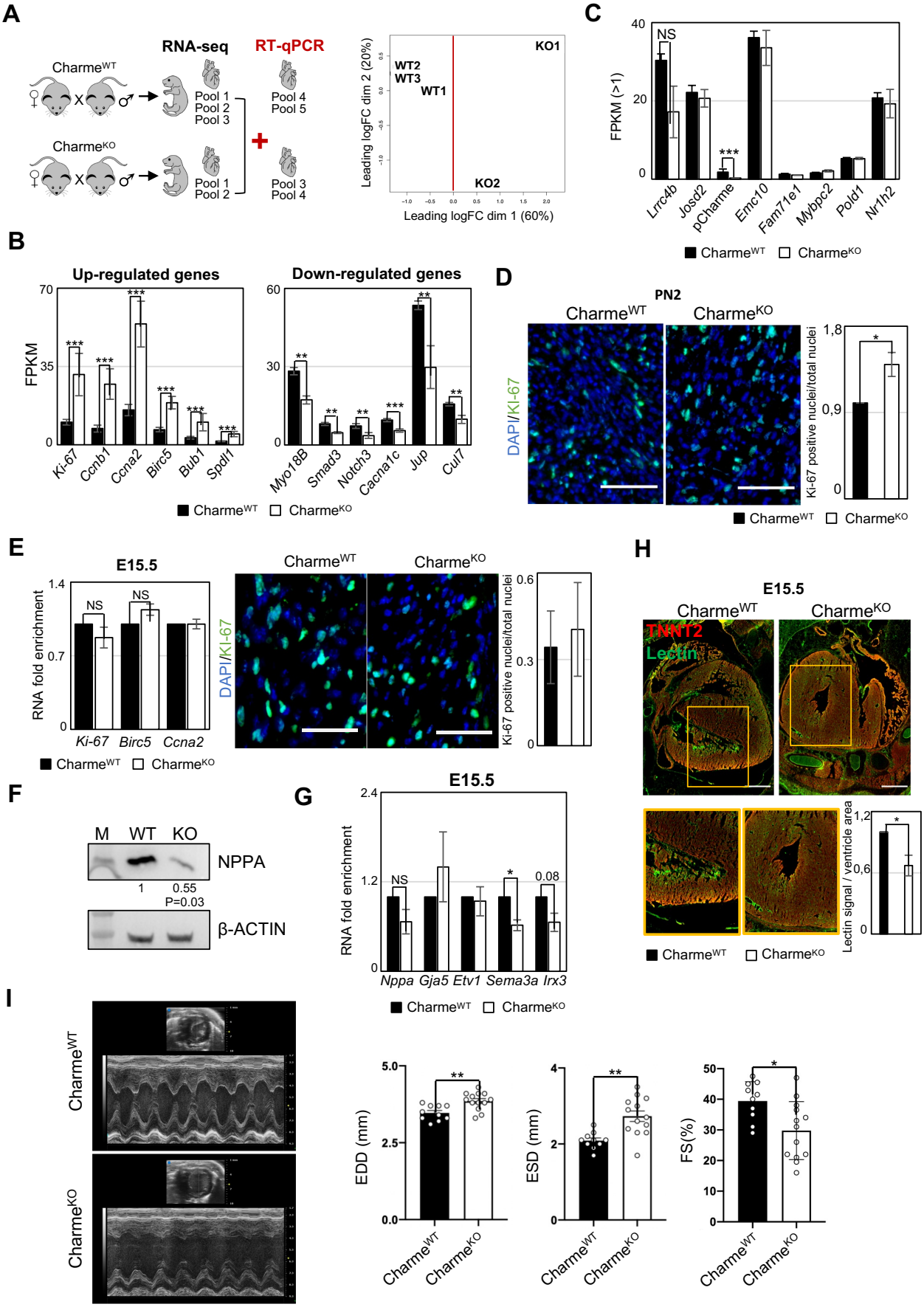

1178

1179 **Figure 2-Figure supplement 1. Related to Figure 2**

1180 **A)** Schematic overview of the workflow to identifying DEGs from Charme^{WT} and Charme^{KO}
1181 transcriptomes (left panel). Multi-dimensional scaling plot of leading fold-change (FC) between each
1182 pair of Charme^{WT} and Charme^{KO} RNA-seq samples (right panel). Plot was obtained by using the
1183 plotMDS function from edger package
1184 (https://www.bioconductor.org/packages/release/bioc/vignettes/edgeR/inst/doc/edgeRUsersGuide.p
1185 df).

1186 **B)** Quantification by RNA-seq (FPKM) of Up-regulated (left panel) and Down-regulated (right panel)
1187 DEGs in Charme^{KO} *vs* Charme^{WT} neonatal hearts.

1188 **C)** Quantification by RNA-seq (FPKM) of pCharme and Charme-neighbouring genes expression in
1189 Charme^{WT} *vs* Charme^{KO} neonatal hearts.

1190 **D)** Left panel: Representative images for KI-67 (green) and DAPI (blue) stainings on Charme^{WT} and
1191 Charme^{KO} neonatal cardiac sections. Scale bars: 70 µm. Right panel: Quantification of KI-67 positive
1192 nuclei/total nuclei on Charme^{WT} and Charme^{KO} cardiac sections from neonatal mice. Data are
1193 expressed as mean ± SEM, n = 4.

1194 **E)** Left panel: RT-qPCR quantification of DEGs belonging to the "cell cycle" GO class from
1195 Charme^{WT} and Charme^{KO} E15.5 hearts. Data were normalized to *Gapdh* mRNA and represent means
1196 ± SEM of n=3 heart pools. Right panel: Representative images for KI-67 (green) and DAPI (blue)
1197 stainings on Charme^{WT} and Charme^{KO} E15.5 cardiac sections are shown. Quantification of KI-67
1198 positive nuclei/total nuclei on Charme^{WT} and Charme^{KO} cardiac sections from E15.5 mice. Data are
1199 mean ± SEM.; n =3. Scale bars: 140 µm.

1200 **F)** Western blot analysis for NPPA in Charme^{WT} and Charme^{KO} E15.5 cardiac extracts. β-ACTIN
1201 was used as a loading control. Quantification of NPPA signal intensity relative to β-ACTIN is shown
1202 below. Data are mean ± SEM (n = 3). *p= 0.03. A representative image is shown.

1203 **G)** RT-qPCR quantification of trabeculae markers expression in Charme^{WT} *vs* Charme^{KO} E15.5
1204 cardiac extracts. Data were normalized to *Gapdh* mRNA and represent means ± SEM of n=3 heart
1205 pools.
1206 **H)** Representative image of Lectin (green) and TnnT2 (red) immunostainings in Charme^{WT} and
1207 Charme^{KO} E15.5 cardiac sections. ROI (orange squares) were digitally enlarged on the lower panels.
1208 Scale bars: 500 µm. Quantification of the area covered by the Lectin fluorescence signal is shown
1209 aside. For each genotype, data represent the mean ± SEM of (at least) 6 images. n=3.
1210 **I)** Representative M-mode echocardiographic track of Charme^{WT} and Charme^{KO} 9-12 months aged
1211 mice. Quantification of heart morphology (EDD= end-diastolic diameter and ESD= end-systolic
1212 diameter) and function (FS: Fractional Shortening =(EDD-ESD)/EDD) were evaluated. Data
1213 represent the mean ± SEM (n = 10-13)
1214 Data information: *$p < 0.05$, **$p < 0.01$, ***$p < 0.001$, unpaired Student's t test.
1215

Figure 3-figure supplement 1

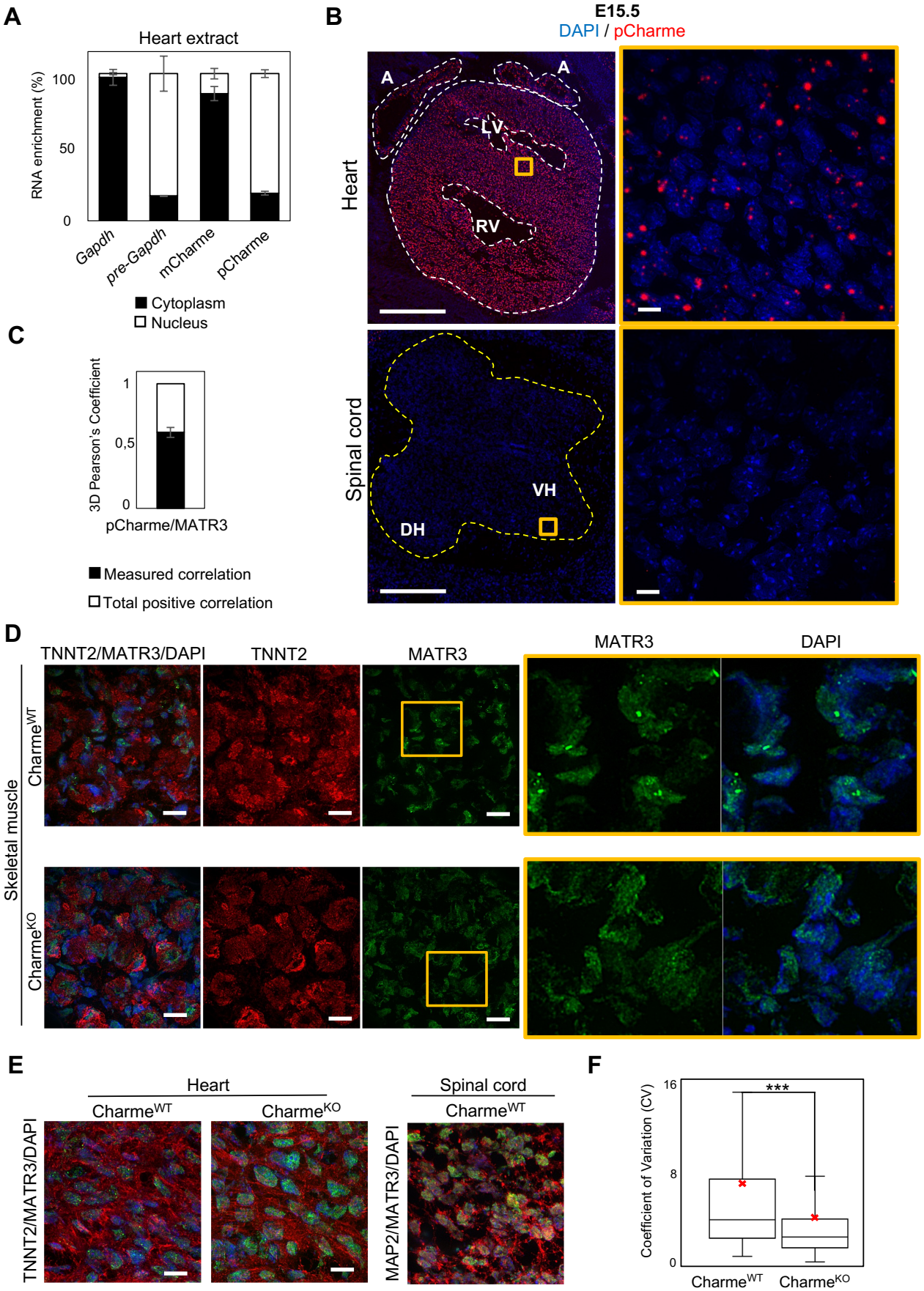

1216

1217 **Figure 3-Figure supplement 1. Related to Figure 3**

1218 **A)** Quantification of the subcellular distribution of pCharme and mCharme in cardiac tissues from
1219 neonatal mice. Histogram shows the quantification by RT-qPCR of the RNA abundance (%) in
1220 cytoplasmic *versus* nuclear compartments. *Gapdh* and *pre-Gapdh* RNAs were used, respectively, as
1221 cytoplasmic and nuclear controls.

1222 **B)** RNA-FISH for pCharme (red) and DAPI staining (blue) in Charme^{WT} hearts and spinal cord from
1223 E15.5 tissue sections (left panels) and their magnification (right panels). Whole heart (white dashed
1224 lines), spinal cord (yellow dashed line). A: Atria; LV and RV: Left and Right ventricle; DH and VH:
1225 Dorsal and Ventral Horn. Scale bars, 500 µm; 10 µm for magnifications.

1226 **C)** 3D Pearson's correlation coefficient of pCharme/MATR3 overlapping signals. Histogram shows
1227 the mean ± SEM calculated over 237 colocalized nuclear signals from 3 independent experiments.

1228 **D)** Representative images for for MATR3 (green), TnnT2 (red) and DAPI (blue) stainings on
1229 Charme^{WT} and Charme^{KO} skeletal muscles from E15.5 tissue sections. ROI (orange squares) were
1230 digitally enlarged on the right panels. Each image is a representative of three individual samples.
1231 Scale bars, 10 µm.

1232 **E)** Left panel: Representative images for for MATR3 (green), TnnT2 (red) and DAPI (blue) stainings
1233 on Charme^{WT} and Charme^{KO} heart from E15.5 tissue sections. Right panel: Representative images for
1234 MATR3 (green), Map2 (red) and DAPI (blue) stainings on Charme^{WT} and Charme^{KO} spinal cord from
1235 E15.5 tissue sections. Each image is a representative of three individual samples. Scale bars, 10 µm.

1236 **F)** Quantification of MATR3 fluorescence intensity distribution (CV=Coefficient of variation) in
1237 Charme^{WT} (N=1346 nuclei) and Charme^{KO} (N=1404 nuclei). The red X indicate the mean value of
1238 CV distribution.

1239

Figure 4-figure supplement 1

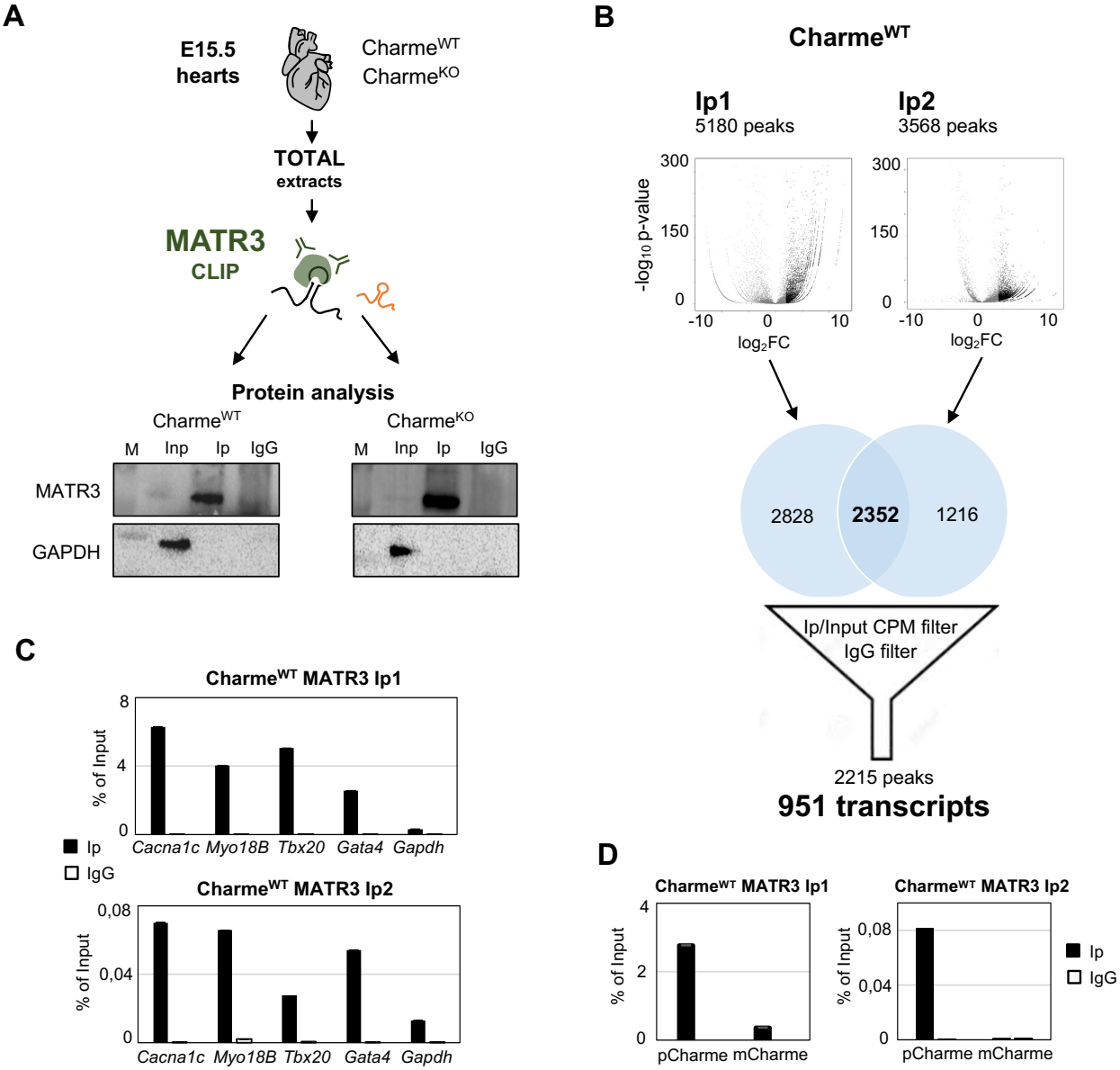

Figure 4-Figure supplement 1. Related to Figure 4

A) Schematic representation of MATR3-CLIP assay as performed from fetal hearts (E15.5) in Charme^{WT} and Charme^{KO} conditions. MATR3 western blot analysis on the retrieved protein fractions is shown. GAPDH protein serves as a loading control. Input (Inp) samples represent 10% of the total protein extracts.

B) Schematic representation of the workflow used for MATR3 CLIP-seq analysis. Volcano plots represent the fold-enrichment over Input ($\log_2$ Fold enrichment, x-axis) and significance ($-\log_{10}$ p-

1248 value, y-axis) of MATR3 peaks in the Ip1 (left panel) and Ip2 (right panel) samples. Black dots
1249 represent the significantly enriched peaks (log_2 Fold enrichment > 2 and FDR < 0.05). Venn diagrams
1250 depict the intersection between Ip1 and Ip2 significantly enriched peaks. The 2215 filtered peaks
1251 correspond to the 951 MATR3-bound transcripts. CPM: Counts Per Million. See Materials and
1252 Methods for details.

1253 **C)** RT-qPCR quantification of *Cacna1c*, *Myo18B*, Tbx20 and *Gata4* RNA recovery in MATR3 Ip1
1254 (upper panel), Ip2 (lower panel) and IgG Charme^{WT} samples. *Gapdh* transcript serves as negative
1255 control. Values are expressed as percentage (%) of Input.

1256 **D)** RT-qPCR quantification of pCharme and mCharme RNA recovery in MATR3 Ip1 (left panel),
1257 Ip2 (right panel) and IgG Charme^{WT} samples. Values are expressed as percentage (%) of Input.

1258

Figure 5-figure supplement 1

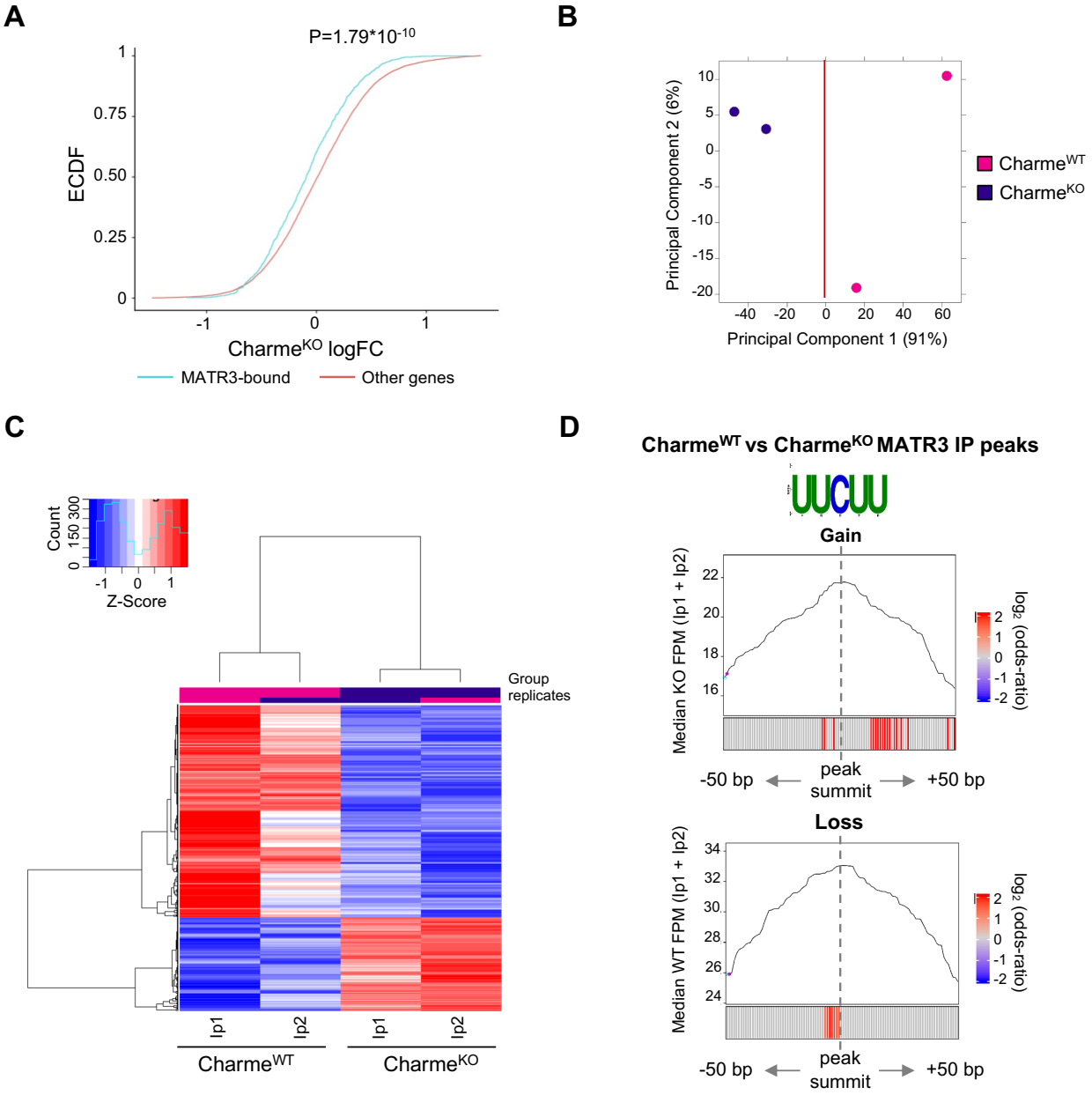

Figure 5-Figure supplement 1. Related to Figure 5

A) Empirical Cumulative Distribution Functions (ECDF) showing the RNA abundance of MATR3 targets in Charme^{KO} condition compared to the other expressed genes. Significance was determined using a two-sided Kolmogorov–Smirnov (KS) test.

B) Principal Component analysis (PCA) plot of Charme^{WT} and Charme^{KO} MATR3 CLIP-seq peaks. Plot was obtained from DiffBind package. See Material and Methods for details.

1266 **C)** Heatmap visualization of Charme^{WT} and Charme^{KO} MATR3 CLIP-seq peaks. Plot was produced
1267 by DiffBind package. Z-Score of normalized reads counts is shown. See Material and Methods for
1268 details.
1269 **D)** Positional enrichment analysis of MATR3 motif in differential MATR3 CLIP-seq peaks
1270 (Charme^{WT} *vs* Charme^{KO}). For each analysed position close to peak summit, line plot displays the
1271 median CLIP-seq signal (FPM, IP1 + IP2) while heatmap displays the $\log_2$ odds-ratio of UUCUU
1272 motif enrichment. Significant enrichments (p-value < 0.05) are shown in red. See Material and
1273 Methods for details. CLIP-seq signal in Charme^{KO} and Charme^{WT} conditions is displayed for «Gain»
1274 and «Loss» peaks, respectively.
1275
1276 **Supplementary File 1. Charme Tss usage data collected from Zenbu genome browser**
1277 **Supplementary File 2. RNA-seq in Charme^{WT} and Charme^{KO} neonatal hearts**
1278 **Supplementary File 3. Ecocardiography measurement for Charme^{WT} and Charme^{KO} animals.**
1279 **Supplementary File 4. MATR3 CLIP-seq in Charme^{WT} and Charme^{KO} fetal hearts**
1280 **Supplementary File 5. List and sequences of the oligonucleotides, siRNAs, antibodies and**
1281 **imaging probes used.**
1282